INORGANIC CHEMISTRY
FRONTIERS

RESEARCH ARTICLE

View Article Online
View Journal

Cite this: DOI: 10.1039/d5qi00648a

Synergistic interplay between oxygen-vacancy and S-scheme charge transfer dynamics in an $LaFeO_3$/FeOOH heterojunction towards sono-assisted photo-Fenton antibiotic degradation and water splitting†

Anshumika Mishra, Newmoon Priyadarshini and Kulamani Parida *

The increasing prevalence of pharmaceutical pollutants in water bodies is a significant threat to public health, and there is a need for a sustainable approach to their remediation. Ultrasound-assisted photo-Fenton reactions are considered the most effective approach for active oxidation processes in sustainable and environmentally friendly remediation. This study represents the step scheme (S-scheme) charge transfer dynamics in FeOOH-anchored $LaFeO_3$ towards the degradation of ofloxacin (OFL) by harnessing ultrasonic waves and simulated solar energy. The heterojunction with intimate interfacial contact and ample oxygen vacancies (O_Vs) was fabricated through a facile two-step sol–gel and *in situ* coprecipitation method. The optimized catalyst attains superior catalytic activity for sono-photo-Fenton OFL degradation (92.3%) with a "k_{app}" of 21.95 min^{-1}, which is 2.19 and 2.05 times higher than pristine semiconductors, and an O_2 evolution rate of 1270 μmol h^{-1} through water splitting. The enhanced catalytic activity is likely ascribed to the facile separation and usage of photogenerated charges through a dynamic S-scheme charge transfer route, the introduction of O_Vs, and continuous charge shuttling between $Fe^{3+/}Fe^{2+}$. Comprehensive characterizations were undertaken to confirm the structural integrity and physico-chemical attributes of the binary heterostructure. EPR, Raman, and XPS studies established the fabrication of O_Vs. Furthermore, the scavenging experiment and EPR analysis confirmed the S-scheme charge transfer pathway. Systematic investigation of various parameters uncovers the catalyst's reaction kinetics, stability, and durability. This dual-function catalyst can be considered a blueprint for the active oxidation process (AOP) for the degradation of toxic environmental pollutants and production of solar fuels.

Received 5th March 2025,
Accepted 20th April 2025

DOI: 10.1039/d5qi00648a

rsc.li/frontiers-inorganic

1. Introduction

Water pollution and energy scarcity are the two major issues gripping the modern-day, rapidly advancing society. They present serious warnings to human health and the ecological equilibrium of the world.[1–3] To combat these issues, various approaches such as photocatalysis, electrocatalysis, and photoelectrocatalysis have been undertaken.[4–6] Among these, the emerging sono-photo-Fenton process is a type of advanced oxidation process (AOP) that synergistically combines sonolysis, photocatalysis, and Fenton reactions to accelerate the degradation of pollutant species *via* the reactive oxygen species (ROS) pathway.[7] Besides, strongly interacting exciton pairs can lead to e^-–h^+ separation, affecting charge carriers and adversely impeding overall catalytic performance.[8] Therefore, achieving effective charge uncoupling and optimizing band positions are accredited as essential factors in enhancing the sono-assisted photo-Fenton reaction (S-P-FR). The use of ultrasound (US) irradiation, along with a custom-made photocatalyst (semiconductor), efficiently removes widely spread non-biodegradable organic toxic pollutants from water bodies. US waves in a liquid medium generate alternating high- and low-pressure zones, leading to the generation of the cavitation phenomenon, which involves the genesis, growth, and collapse

Centre for Nano Science and Nano Technology, S 'O' A (Deemed to be University), Bhubaneswar-751 030, Odisha, India. E-mail: kulamaniparida@soauniversity.ac.in, paridakulamani@yahoo.com

† Electronic supplementary information (ESI) available: Formation of O_Vs in LFO and FeOOH (Scheme-S1); band offset at the LFO/FeOOH heterointerface (Scheme-S2); average particle size determination (Fig. S1); color mapping and EDAX spectra of nanocomposite LF13 (Fig. S2); XPS survey spectra for LFO, FeOOH, and LF13 (Fig. S3); BET surface area and pore size analysis (Fig. S4); work function plot (Fig. S5); catalytic absorbance spectra (Fig. S6); stability proof of the catalyst (Fig. S7); point of zero charge (PZC) and pK_a of the ofloxacin plot (Fig. S8); control experiment plots of OFL degradation efficiency (Fig. S9). See DOI: https://doi.org/10.1039/d5qi00648a

of local short-lived microbubbles and supercritical areas within the medium. The collapse of these microbubbles generates high local temperatures and pressures (reaching over 1800 kPa and ~5000 °C) and reactive oxygen species (ROS) such as $HO^{\bullet}$ and $O_2^{\bullet-}$ through a molecular oxygen activation (MOA) process and cleavage of the H_2O molecule. During the rapid cooling phase, these radicals react with each other and undergo a reaction with O_2 and H_2O, creating a highly reactive environment capable of oxidizing or reducing inorganic pollutants.[9] Besides, S-P-FR is a novel approach that harnesses the unique benefits of ultrasound (US), UV-visible light irradiation, and the Fenton reaction (Fe^{2+}/H_2O_2) to produce highly reactive $^{\bullet}OH$ (oxidizing E_o = 2.73 eV), powerful oxidizing agents that can break down a wide array of persistent contaminants.[7] The core principle of the Fenton reaction involves the catalytic decomposition of H_2O_2 by Fe^{2+} ions in an acidic medium to produce additional $^{\bullet}OH$, which can oxidize organic pollutants to a less/non-toxic form. The production of a significant amount of $^{\bullet}OH$ radicals demonstrates a substantial capability for the non-selective oxidation (degradation) of organic compounds, occurring through a series of reactions. When combined with US and light irradiation, the efficiency of the process is significantly enhanced. Simultaneously, photo-irradiation accelerates the production of $^{\bullet}OH$ by photolyzing H_2O_2 and regenerating Fe^{3+} ions.[9]

This calls for the development of smart photocatalysts such as perovskites,[10] graphene,[11] LDH,[12] MOF,[13] MXene,[14] quantum dots,[15] metal sulfides,[16] and metal oxides[17] with enhanced catalytic efficiencies. Nanomaterials like $LaFeO_3$ (LFO), a visible active perovskite, have generated significant excitement owing to their intriguing physicochemical, optoelectronic, pyroelectric, ferroelectric, superconductive, and piezoelectric features, which are extensively used in various applications, especially in heterogeneous catalysis.[18] Furthermore, LFO can serve as a potential Fenton catalyst, more precisely as a peroxide activator using the Fe^{3+} and Fe^{2+} redox cycle.[19] The Fe^{2+}/Fe^{3+} redox cycle can be accelerated by creating surface atomic vacancies (oxygen), aiding in improved S-P-FP activity. O_V are responsible for inducing defect states in the semiconductor (SC) matrix that act as electron traps, enhancing active adsorption and activation sites, rendering engineered band gaps, increasing redox potentials, and being effective towards pollutant degradation. Besides, the induced lattice distortions in the SC matrix add to the active site's stability and the robustness of the SC.[20]

Recently, several studies have been reported on using LFO as a photocatalyst in the presence of an oxidant. Photo-Fenton removal of TC-HCl using LFO yielded a quite appealing degradation efficiency within 1 h under optimal conditions.[21] Similarly, US-assisted Fenton-type mineralization of 4-chlorophenol using LFO yielded five times higher degradation results compared with the individual AOPs.[22] However, individual photocatalyst systems often fall short in delivering optimal catalytic performance due to limited exciton separation, restricted light absorption range, and the short-lived nature of photogenerated charge carriers. As a solution to this, the concept of heterojunction formation (such as type I, type II, Z-scheme, S-scheme) comes into play as a key engineering strategy to enhance charge separation and transfer efficiency. Besides, this strategy tends to introduce material stability along with enhancing structural, morphological, and optical properties.[23–27] To conquer these hurdles concerning LFO, a heterojunction is put up by the integration with an additional semiconductor such as FeOOH (iron oxyhydroxide). FeOOH is deemed suitable to be paired with LFO due to its light absorption properties and favorable VB-CB positions. Owing to its promising n-type nature with E_g ~1.5–1.9 eV, FeOOH is widely applicable in catalytic processes and energy-harvesting gadgets.[28–31]

In this work, we have designed a novel binary n–n heterojunction (LFO@FeOOH) *via* a combination of sol–gel and *in situ* co-precipitation techniques (Scheme 1). The engineering of S-scheme charge transfer dynamics, US irradiation, and Fenton reaction mechanisms leverages synergistic sono-photo-Fenton degradation of OFL alongside sonophotocatalytic OER through water splitting. The synergistic methodology fosters strong interfacial contact and optimized charge carrier migration between the two semiconducting materials while promoting uniform nanocomposite formation with enhanced structural stability and catalytic performance. The ROS generated through the MOA process is thoroughly examined in the context of its influence by simulated solar irradiation and US vibrations, which simultaneously facilitates efficient charge separation, mass transfer kinetics, and catalyst dispersion. The accelerated Fe^{2+}/Fe^{3+} cycle sustains the continuous Fenton activity for enhanced $^{\bullet}OH$ radical production. Furthermore, the US cavitation enhances the mass transfer, catalyst dispersion, and ROS generation, amplifying the degradation efficiency.

The successful construction of the $LaFeO_3$@FeOOH heterojunction with controlled O_Vs and an S-scheme charge transfer dynamics has demonstrated remarkable potential for advanced environmental (OFL degradation) and energy applications (OER from water splitting). The intimate interfacial contact between $LaFeO_3$ and FeOOH not only enhances charge carrier separation through the formation of a directional S-scheme heterojunction but also preserves the strong redox potentials of exciton pairs. The combined roles of O_V-assisted charge dynamics, S-scheme interfacial engineering, and sono-photo-Fenton activation highlight a robust strategy for designing multifunctional catalysts. The combined influence of an internally generated electric field, the sonication process, and the Fenton environment facilitates efficient charge separation and migration toward the catalyst's surface. The sono-photo-Fenton process combines light irradiation, ultrasonic effects, and the Fenton mechanism to maximize ROS generation, including $^{\bullet}OH$ and $^{\bullet}O_2^-$.

2. Results and discussion

2.1. Material characterization

HRTEM analysis of the morphology of the FeOOH@$LaFeO_3$ composite validated the nucleation of FeOOH nanorods (NRs),

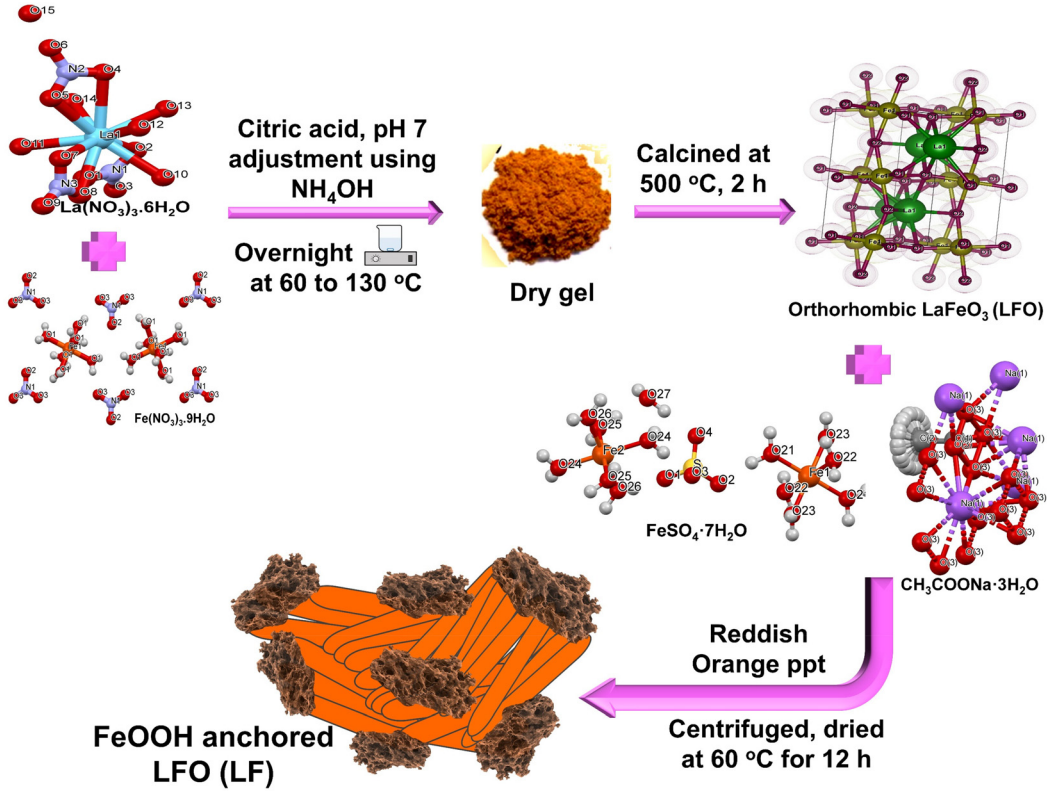

Scheme 1 Method of LF13 fabrication using sol–gel and *in situ* coprecipitation methods.

with an average particle size of ~65 nm (LFO) and 407 nm (FeOOH) (Fig. S1a and b†) over the surface of agglomerated nanostructured LFO and the intimate interfacial contact, as illustrated in Fig. 1a. Besides, Fig. 1b depicts close interfacial contact between the pristine material (yellow dotted line), suggesting binary heterojunction formation. Moreover, the HRTEM fringe pattern image of the composite (LF13, particle size ~110 nm, Fig. S1c†) exhibits a *d*-spacing of 0.295 nm and 0.23 nm assigned to (121) and (021) planes of LFO and FeOOH, respectively.[32,33] Fig. 1c depicts the FFT patterns corresponding to the *d*-spacing images of the LF13 composite, where the yellow circle in the FFT pattern image depicts the presence of surface unsaturation arising out of missing atoms at their sites (O_v).[34–36] The circular diffraction spots monitored in the SAED pattern reveal the polycrystallinity character of the hetero-nanostructures (Fig. 1d). Moreover, the color elemental mapping (Fig. S2a†) and EDX (Fig. S2b†) confirm the purity and uniform elemental distribution of the constituent elements (La, Fe, O) in the synthesized nanocomposite. The FESEM image of the LF13 composite and LFO is pictured in Fig. 1e and f, respectively.

The XRD patterns are presented in Fig. 2a, with peaks indexed at (101), (121), (220), (202), (141), (240), and (242) crystal planes correspond to the orthorhombic LFO nanostructures (consistent with JCPDS File: 37-1493)[37] having an average crystallite size of 20.76 nm, with the *Pnma* space group with lattice parameters of a = 5.56 Å, b = 7.85 Å, and c = 5.55 Å, indicating the absence of any contamination phases. Moreover, all the characteristic peaks for FeOOH are viewed at (020), (310), (031), (051), (151), and (231) corresponding to the orthorhombic state of γ-FeOOH (lepidocrocite, consistent with JCPDS card no. 74-1877) having a ~28.74 nm crystallite size.[38,39] Additionally, the XRD patterns of the composite closely match those of the parent LFO and FeOOH, indicating the uniform nucleation of LFO nanoparticles over FeOOH nanorods. The absence of impurity peaks rules out the possibility of secondary phase formation, which suggests the formation of a binary heterojunction.[40] This was additionally confirmed with the help of EDAX (Fig. S2b†), HRTEM fringe patterns (Fig. 1b), and XPS survey spectra (Fig. S3c†).

The elemental content and valence states of the surface LFO nanoparticles were analyzed using X-ray photoelectron spectroscopy (XPS). The appearance of La(3d), Fe(2p), and O(1s) is evident from the survey spectra of LFO, FeOOH, and LF-13 nanoparticles (Fig. S3†). The deconvolution of the individual high-resolution La 3d, Fe 2p, and O 1s spectra was carried out using Casa XPS software. The deconvoluted La 3d spectra (Fig. 2b) also yielded six fitted peaks for LFO and LF13. For LFO, the observation of two sets of peaks at lower binding energy (BE), *i.e.*, at 833.78, 835.10, and 838.32 eV, is attributed to $3d_{5/2}$ and two satellite peaks, respectively, and the peak set at a higher BE of 852.07, 847.47, and 855.17 eV is attributed to $3d_{3/2}$ and two satellite peaks. For LF13, 830.12, 834.57 and 838.13 eV denote $3d_{5/2}$ and two satellite peaks, respectively,

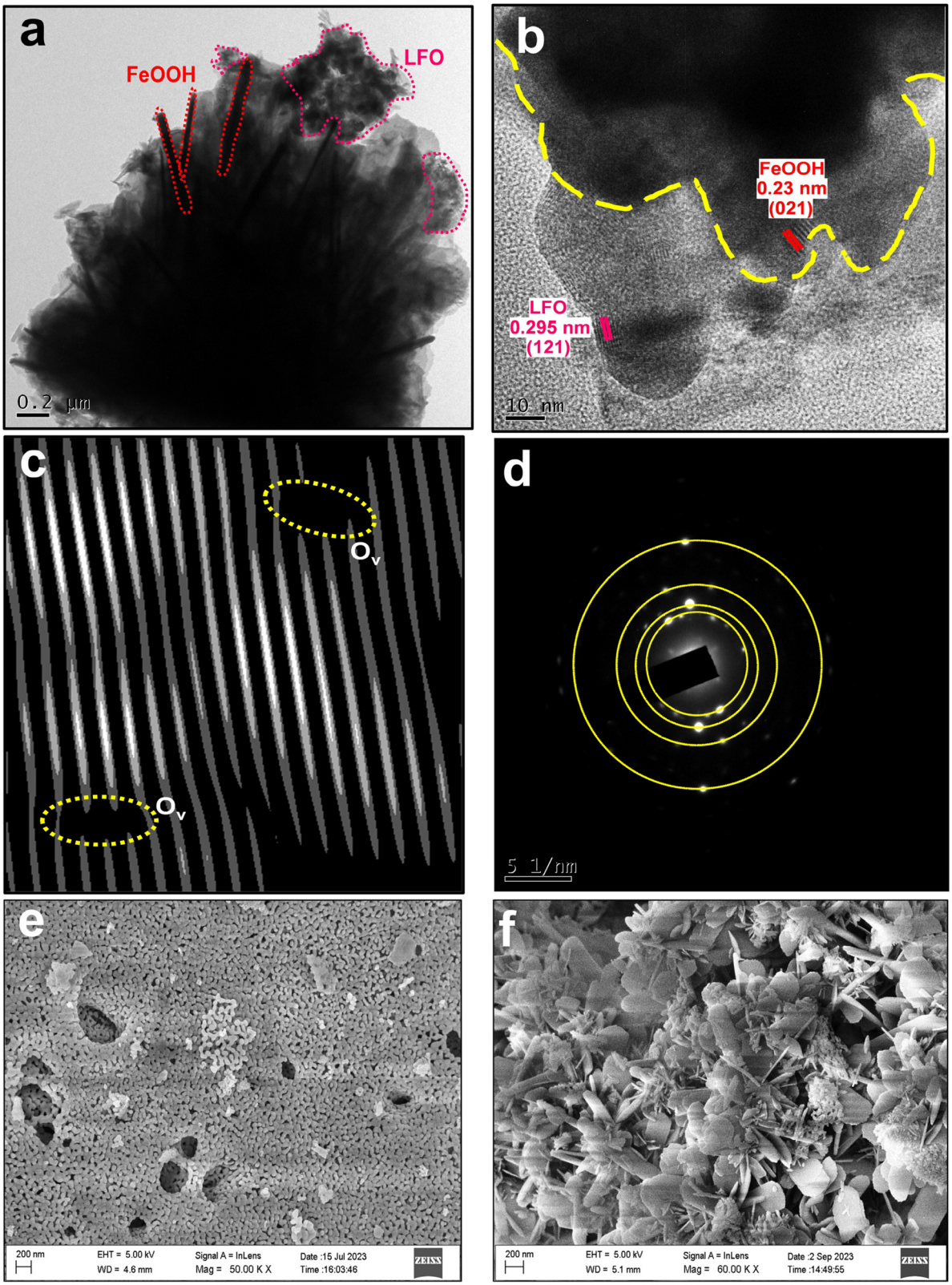

Fig. 1 (a and b) HRTEM image of the LF13 composite with intimate interfacial contact. (c) Inverse FFT pattern of LF13 showing the presence of O_v. (d) SAED pattern of the LF13 composite and (e and f) FESEM image of LF13 and LFO.

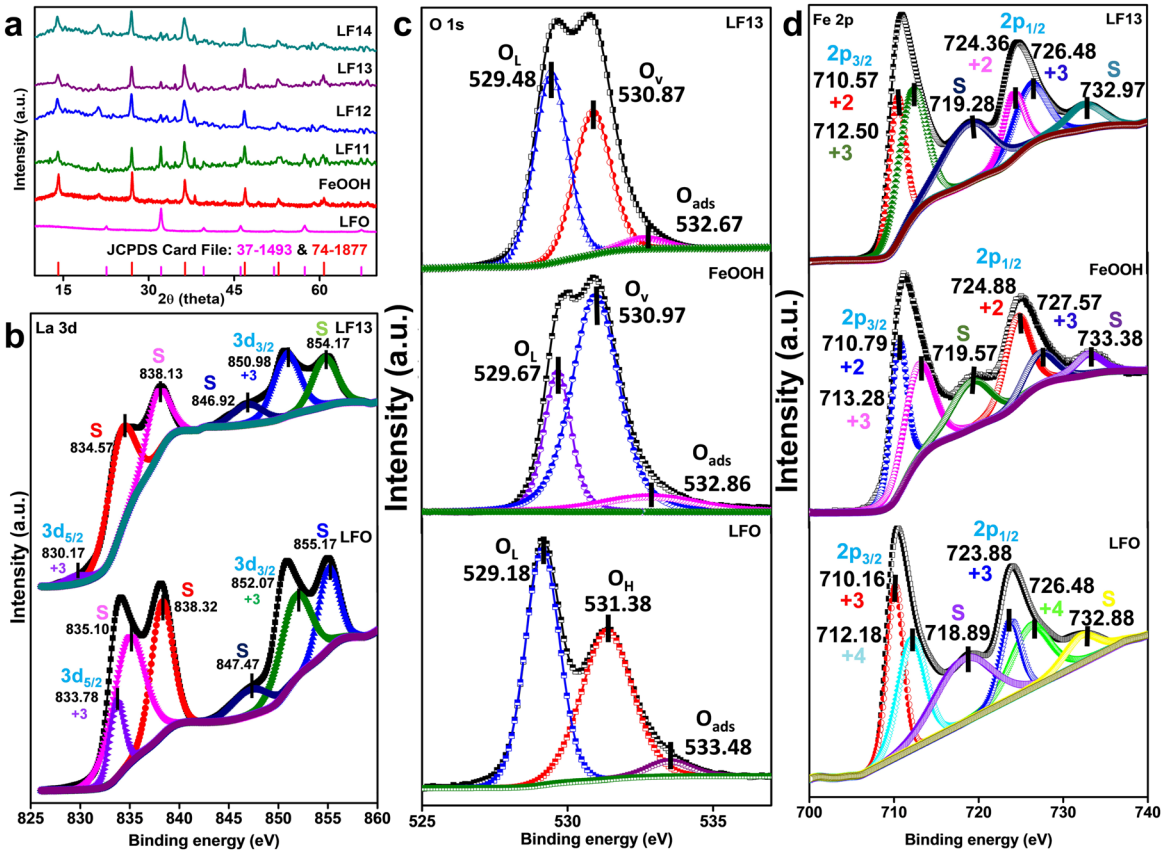

Fig. 2 (a) PXRD spectra of LFO, FeOOH, and the various nanocomposites (LF) with varied molar ratios. Deconvoluted XPS spectra of (b) La 3d, (c) O 1s and (d) Fe 2p for LFO, FeOOH, and LF13.

whereas 850.98, 846.92 and 854.17 eV correspond to the $3d_{3/2}$ and two satellite peaks, respectively. A significant difference between the BE of $3d_{5/2}$ and $3d_{3/2}$ suggests the presence of La^{3+} in the LFO matrix.[41] The O 1s spectra upon deconvolution displays three peaks for each of LFO, FeOOH, and LF13 (Fig. 2c). The peaks at 529.18 eV (LFO), 529.67 eV (FeOOH), and 529.48 eV (LF13) correspond to the presence of crystal lattice oxygen bonds of La–O and Fe–O (O_L). For LFO, the peak at 531.38 eV corresponds to the surface hydroxyl oxygen presence, while 530.97 eV (FeOOH), and 530.87 eV (LF13) are attributed to the non-lattice ionic oxygen associated with O_V. In contrast, 533.48 eV (LFO), 532.86 eV (FeOOH), and 532.67 eV (LF13) correspond to the weakly bound surface adsorbed oxygen (O_{ads}) species such as $^{\bullet}OH$ and $^{\bullet}O_2^-$.[42] A decrease in the O_V is detected in the composite compared with FeOOH. The presence of O_V, confirmed by the EPR results, enhanced the activity of the composite. In contrast, excess O_V retards the reaction by acting as an electron-trapping site, and reduced O_V makes the composite defect free, affecting its activity. Hence, O_V can be considered a "necessary evil" to enhance the activity of the composite.[43] The Fe 2p spectra deconvoluted to six peaks for all the neat and composite materials. For LFO, the Fe $2p_{3/2}$ and $2p_{1/2}$ (Fig. 2d) are indexed at 710.16 and 723.88 eV (with satellite peaks at 718.89 and 732.88 eV). For FeOOH, the Fe $2p_{3/2}$ and $2p_{1/2}$ are at 710.79 and 724.88 eV (with satellite peaks at 719.57 and 733.38 eV), whereas, the Fe $2p_{3/2}$ and $2p_{1/2}$ are indexed at 710.57 and 712.50 eV in the case of LF13, with satellite peaks at 719.28 and 732.97 eV. The peak fittings suggest the presence of mixed valence states of Fe (+3 and +4) in LFO due to the loosely bound oxygen species on the Fe^{3+} site.[44] Also, Fe deficiency appears due to the transformation of Fe^{3+} to Fe^{4+}, which is evident in the presence of O_V, reducing the activation energy, and facilitating the charge carrier recombination, resulting in reduced activity. The addition of FeOOH (presence of +2 and +3 valence states) aids in overcoming the Fe deficiency and also introduces O_V into the composite, enabling Fe^{3+} to Fe^{2+}, resulting in varied degrees of deviation owing to the different levels of interaction between the Fe mixed valence states, and O atoms of FeOOH.[42,44] In short, the peak shifting depicted in La 3d, Fe 2p, and O 1s of the LF13 composite substantiates the intensive interaction along with heterojunction formation between LFO and FeOOH. Thus, nucleating FeOOH nanorods over LFO nanoparticles expedites the formation of strong surface interactions that drive efficient charge separation and migration. The acquired XPS data confirms the presence of the LF13 binary composite, consistent with the XRD and EDX outcomes.

The Raman spectra of pristine and composite materials are shown in Fig. 3a–c. LFO with a orthorhombic *Pnma* space

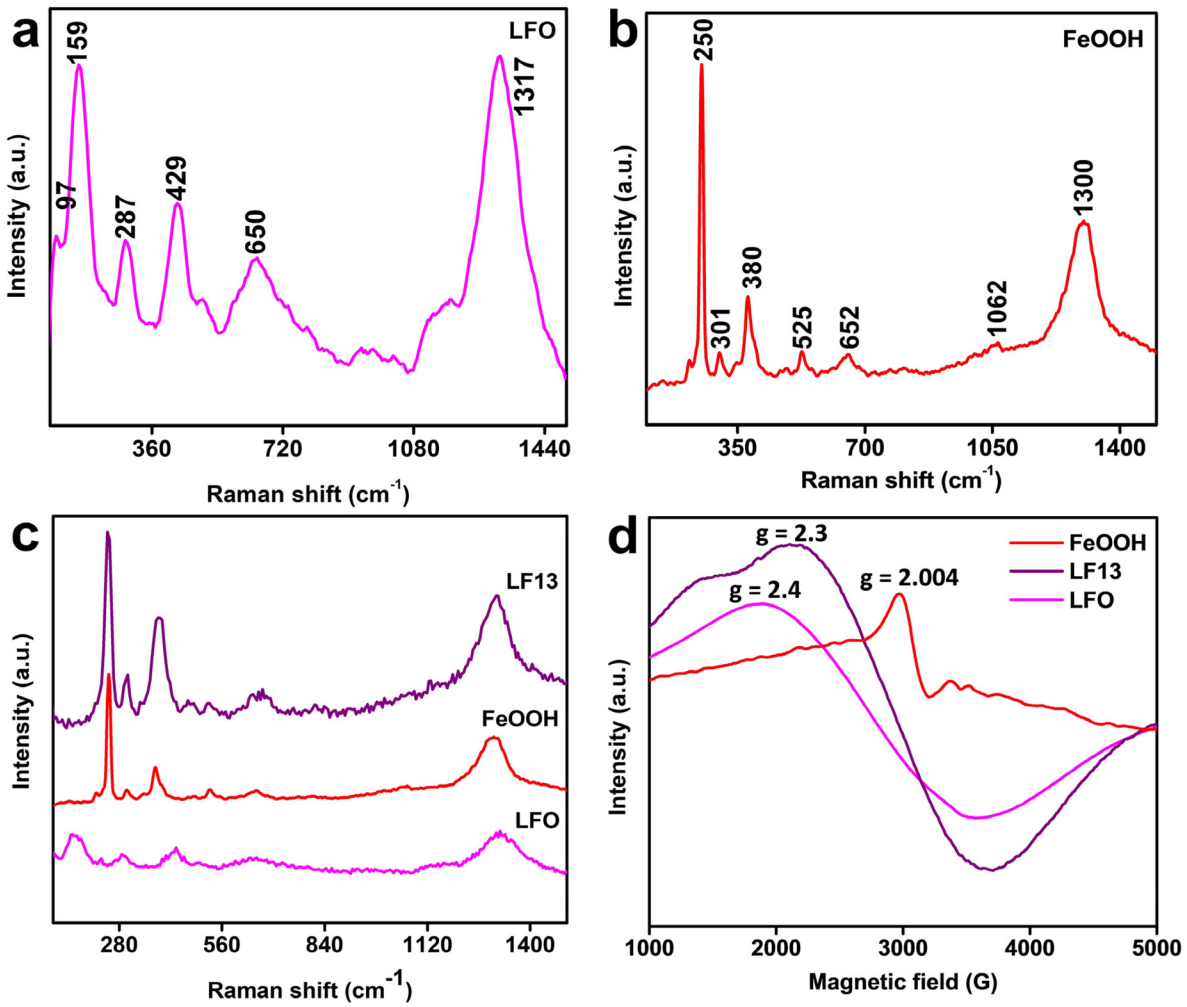

Fig. 3 Raman spectra of (a) LFO, (b) FeOOH, and (c) stacked LF13 and pristine materials, (d) EPR spectra of LFO, FeOOH, and LF13 with their corresponding *g*-values.

group normally exhibits 24 Raman active modes at room temperature as per reports.[45,46] However, establishing all the modes is tough for complex LFO oxides. The Raman spectra of pristine LFO were recorded in the 50–1500 cm^{-1} range, where six signal peaks were observed for LFO positioned at 97, 159, 287, 429, 650, and 1317 cm^{-1}. Of them, the signal peaks at 650 and 1317 cm^{-1} showcase double (two) photon scattering, and the rest exhibit mono photon scattering. The signal peaks at 97 cm^{-1} correspond to the B_{1g} mode, 159 cm^{-1} correspond to the La–O vibrations, and 287 and 429 cm^{-1} depict the La–O A_g mode and B3 g mode of Fe–O, respectively. The above modes also correspond to the tilted and bending vibrations of the FeO_6 octahedra. The signal peak at 650 cm^{-1} is attributed to the B_{1g} symmetric stretching mode and basal oxygen of the octahedra.[45] For pristine FeOOH, distinct bands are identified at 250, 301, 1300, 525, 652, 1062, and 1380 cm^{-1}, which correspond to the fundamental Raman modes, associated with asymmetric stretching vibrations of metal–oxygen hydroxyl groups.[28,38] For the composite LF13, these characteristic peaks of the individual components exhibit significant shifts in position and changes in intensity, reflecting strong interactions between the two constituents. The increased intensity of the LFO peaks and reduced intensity of FeOOH peaks in the composite's Raman spectra suggest the optimal presence of oxygen vacancies, contributing to improved photocatalytic performance.

To further validate the presence of defect states (surface O_V), an EPR analysis was conducted, and the obtained result is shown in Fig. 3d. The *g*-values are calculated using the following equation:

$$g = \frac{h\nu}{\beta H} \quad (1)$$

where h, ν, β, and H denote their conventional meaning. The obtained *g*-value for LFO is 2.4 owing to the defect state arising in the La-based perovskites.[47] For FeOOH, the obtained *g*-value (2.004) signifies the presence of a paramagnetic center,[29] where an electron departed from O_V is confined near the surface of the Fe^{2+}/Fe^{3+} redox pair to Fe^{3+}–VO–Fe^{4+}. In LF13, an

observed signal around g = ~2.3 is ascribed to the presence of surface O_V for LFO and FeOOH. The presence of O_Vs for LFO and FeOOH is pictured well in Scheme S1.†

The surface area (SA) and distribution of pore sizes of a catalyst are the key factors that determine the effectiveness of the fabricated catalyst towards adsorption and photocatalysis abilities.[48] The determination of surface area, along with pore size distribution, was undertaken, encompassing the Brunauer–Emmett–Teller (BET) and the Barrett–Joyner–Halenda (BJH) analysis, respectively, where Fig. S4† exemplifies the superficial characteristics of LFO, FeOOH, and LFO/FeOOH through the N_2 adsorption–desorption isotherm method. A type-IV adsorption isotherm is observed for the pristine and the nanocomposite, showcasing a characteristic H3 hysteresis loop that indicates a characteristic mesoporous material.[49] LF13 exhibited a mesoporous surface with a diameter of 3.805 nm and a BET SA of 109.186 $m^2\ g^{-1}$. In contrast, LFO and FeOOH exhibited pore diameters of 3.076 and 3.837 nm, respectively, with BET SA of 38.668 and 98.517 $m^2\ g^{-1}$, respectively, showcasing a boost in the overall surface area of the neat LFO following modifications with the FeOOH mixed phases. Additionally, the *in situ* preparation of the nanocomposite helps in the formation of finer-sized crystallites that naturally have increased surface area due to a higher surface-to-volume ratio. Hence, the composite displayed higher adsorption capabilities and increased active sites owing to the presence of mesoporosity and finer crystallite sizes, and improved BET SA, which significantly boosted photocatalytic activity.

The light-absorbing characteristics and band structure of the photocatalysts examined using the UV-Vis diffuse reflectance spectroscopy (UV-vis DRS) study illustrate the strong absorption in the 200–800 nm range (Fig. 4a) relevant to the dark and metallic nature of LFO, with an absorption edge around 640 nm arising from the electronic transition between VB and CB ($O_{2p} \rightarrow Fe_{3d}$). Meanwhile, FeOOH and the composites absorb in the UV and visible regions. The absorption spectra of the composites and the pristine materials suggest that the prepared photocatalysts absorb in the visible light region and can potentially serve as visible light active photocatalysts towards the degradation of organic pollutants. The optical band gaps (E_g) of the materials were determined from the Tauc plot (Fig. 4b and c) using the Kubelka–Munk function, and were calculated to be 1.89 eV for LFO and 1.95 eV for FeOOH, aligning well with earlier reported values in the literature.[38,50] The calculated flat band potentials (E_{fb}) of pristine materials derived from the Mott–Schottky plot (Fig. 4d and e) were found to be −0.73 and −0.51 V for LFO and FeOOH, respectively, suggesting their n-type semiconductor characteristics. Furthermore, VB XPS analysis (Fig. 4f and g) revealed the VB edge positions of LFO and FeOOH to be 1.35 eV and 1.62 eV, respectively. From the above details, the calculation of the CB potential for LFO and FeOOH using the following equation,

$$E_{CB} = E_{VB} - E_g \quad (2)$$

suggested a value of −0.54 and −0.33 eV, respectively, indicating that $E_{CB_{LFO}}$ is more negative compared with $E_{CB_{FeOOH}}$. Following numerous reports, the Fermi level (E_f) in n-type semiconductors is typically 0.1–0.2 V lower than the E_{CB}.[51] Therefore, the E_f for LFO and FeOOH were measured to be −0.44 and −0.23 eV, respectively. Additionally, VB-XPS was employed to evaluate the work functions.[52,53] The work functions (ϕ) of LFO and FeOOH were determined using the following equation:

$$\Delta V = \phi - \varphi \quad (3)$$

where φ represents the work function of the XPS instrument (set to ~4.2 eV), and ΔV stands for the contact potential difference. ΔV is derived by measuring the difference in BEs between the spectrum's two inflection points (IPs) (Fig. S5†). Using the equation above, the ϕ of LFO and FeOOH were noted to be 6.78 eV and 7.24 eV, respectively.

2.2. Evaluation of catalytic activity

2.2.1. Sono-photo-Fenton ofloxacin degradation. The sono-Fenton (SF), photo-Fenton (PF), and sono-photo-Fenton (S-P-FR) activity of the prepared catalysts are assessed based on ofloxacin degradation, employing the molecular oxygen activation method by exposing the reaction systems individually to US vibrations (SF), simulated light (PF), and both US vibrations and simulated light (S-P-FR). The eventual reduction in the characteristic absorbance hump of ofloxacin (OFL) at λ_{max} ~289 nm is an explicit confirmation of its quantitative degeneration.[54] Following the PF reaction, the ofloxacin degradation order from highest to lowest is LF12 (58%) > LF11 (54%) > LF13 (50%) > FeOOH (45%) > LF14, LFO (42%) due to the vast light harvesting ability of the FeOOH and the formed nanocomposites. In the case of the SF reaction, the degradation order follows the trend LF11 (54%) > LF12, LFO (50%) > LF13 (47%) > FeOOH (45%) > LF14 (40%). As such, the US plays a dual role as a catalyst as well as a reactant, where the reactant facilitates pollutant degradation through sonolysis by the generation of oxidizing free radicals such as hydroperoxy and hydroxyl, and promotes oxidative degradation as a catalyst. Besides, the disruption of cavitation bubbles produces shock waves, which enhance the catalyst dispersion and raise the catalyst surface temperature, accelerating the reaction rate. Furthermore, cavitation results in the formation of a highly reactive, unpassivated surface. A complete reversal of the degradation order is observed upon combining the US and photoirradiation in the S-P-FR, which reads as LF13 (92.3%) > LF12 (82%) > LF14 (80%) > LF11 (70%) > FeOOH (65%) > LFO (55%). The observed catalytic activity (SF/PF/S-P-F) is illustrated in Fig. S6.† The kinetic studies of the observed catalytic activity towards OFL degradation (Fig. 5a–c) are investigated using the Langmuir–Hinshelwood model, details of which are mentioned in Text S7. The rate constant (k_{app}) value was derived as the slope of the $\ln(C_o/C_t)$ *vs.* time (t) plot depicted in Fig. 5d–f, based on pseudo-first-order kinetics. The calculated k_{app}, R^2, and $t_{1/2}$ values for the materials are summarized

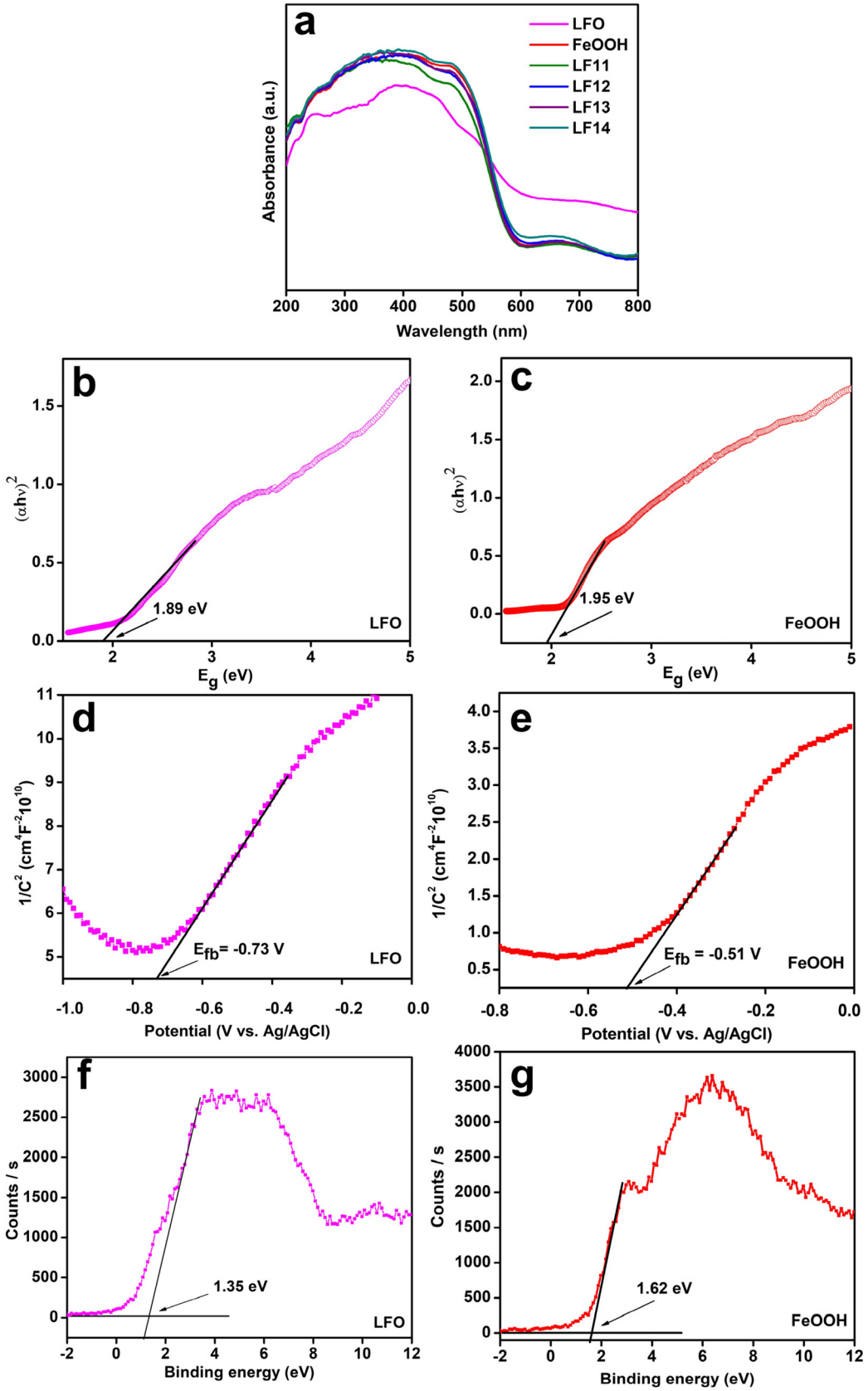

Fig. 4 (a) UV-DRS spectra of the pristine and nanocomposites. (b and c) Tauc plot, (d and e) M–S plot, and (f and g) VB XPS plot of LFO and FeOOH.

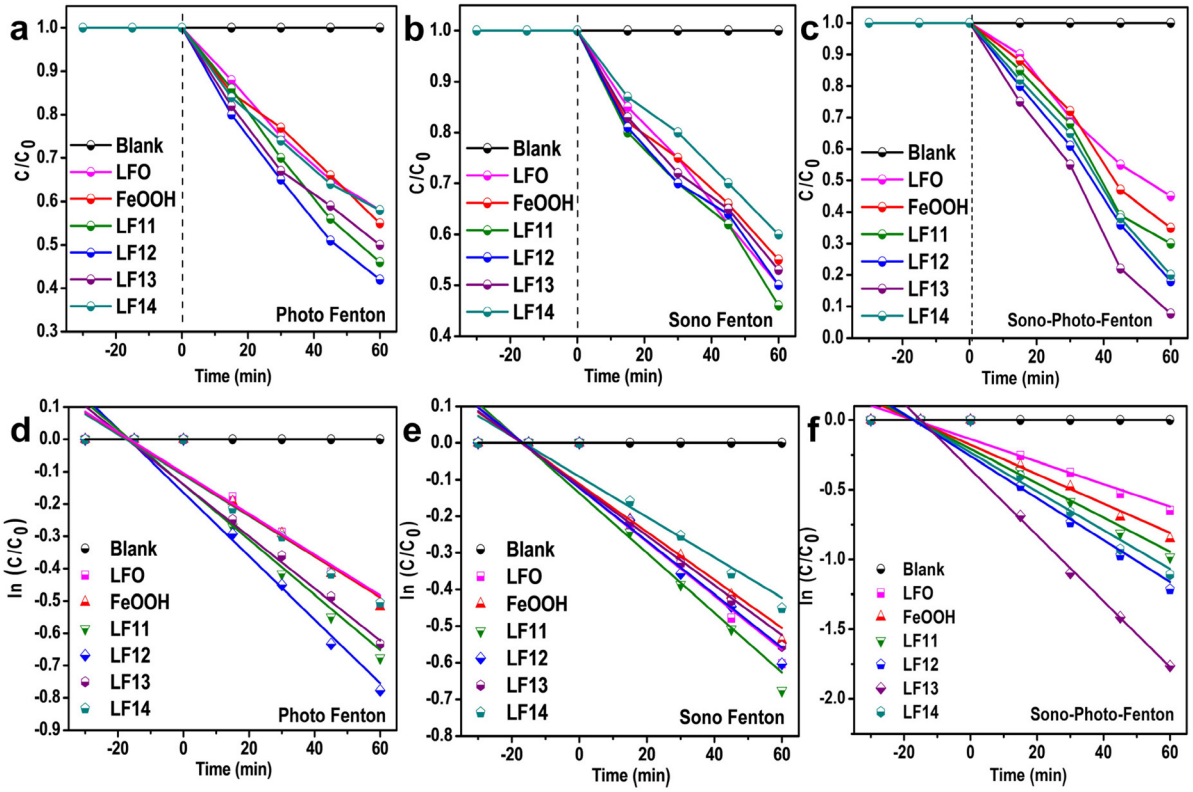

Fig. 5 (a–c) Relative concentration curve for OFL degradation and (d–f) its corresponding kinetics plot using pristine and nanocomposite materials following the Langmuir–Hinshelwood model.

in Table S1,† where LF13 shows a degradation efficiency of 92.3%, and exhibits k_{app} ~21.95 × 10^{-3} min^{-1}, R^2 = 0.913, and $t_{1/2}$ = 32 min.

Further, the generation of ROS, accountable for driving the catalytic reaction on the surface of the composite, is confirmed through scavenger tests, TA-PL, and NBT, as depicted in Fig. 6. The results of the scavenger test suggested that $^{\bullet}OH$ and $^{\bullet}O_2^-$ were the primary ROS upon validation using the NBT and TA-PL test. Besides, sono-photo-Fenton degradation of OFL is subjected to various operational parameters such as anion and cation study, gas purging, pH variation, and the oxidizer effect, using the best nanocomposite LF13. The order of viewed reactivity is as follows: $Cl^- > NO_3^- > CO_3^{2-}$, $K^+ > Ca^{2+} > Mg^{2+}$; Ar > N_2 > O_2, H_2O_2 > $K_2S_2O_8$; and pH 5 > pH 7 > pH 3 > pH 9 (Fig. 7a–e). The reasons attributed to the observed trends are elaborated in the ESI (Text S5†).

Additionally, the reusability and stability of the nanocomposite LF13 are crucial factors in water treatment methods, where LF13 was subjected to five consecutive experiments (Fig. 7f). The OFL removal efficiency decreased by less than 10% after the fifth cycle, indicating the catalyst's strong reusability, as confirmed by post-experimental analysis of the nanocomposite through XRD, TEM, and UV analysis (Fig. S7†). The LC-MS analysis monitored the intermediary species formed during the catalytic reaction (Scheme 2). Additionally, a total organic carbon (TOC) was measured at 79% after 1 h, with the remaining percentage likely attributed to small molecular intermediates, as corroborated by the LC-MS results. Moreover, no ROS generation (responsible for OFL degradation) was detected with light and US irradiation, but without a catalyst, and with the catalyst but without light (dark conditions) and US irradiations, as depicted in Fig. S9.† This confirmed that both light and ultrasonication, along with the catalyst, are essential for degrading OFL. Also, OFL does not absorb light and US irradiations to undergo self-photolysis or sonolysis, respectively.

2.2.2. Sonophotocatalytic OER from water splitting. The OER performance of LF13 was evaluated for the sluggish four-electron water oxidation reaction under sono-, photo-, and sonophotocatalytic conditions using water and sacrificial agents such as $FeCl_3$ and $AgNO_3$ (Fig. 8a and b). In sonophotocatalysis, the highest OER rates were observed as 1270 μmol h^{-1} and 965 μmol h^{-1} for $FeCl_3$ and $AgNO_3$, respectively, which were higher compared with photocatalysis (730 μmol h^{-1} for $FeCl_3$ and 390 μmol h^{-1} for $AgNO_3$) and sonocatalysis (112 μmol h^{-1} for $FeCl_3$ and 94 μmol h^{-1} for $AgNO_3$). This demonstrates the pivotal role of piezo-polarization in enhancing the photocatalytic activity of the binary composite. A comparative OER activity plot is depicted in Fig. 8c.

Compared with $AgNO_3$, the superior activity in the $FeCl_3$ solution is ascribed to the reduction of Fe^{3+} to Fe^{2+} by photo-

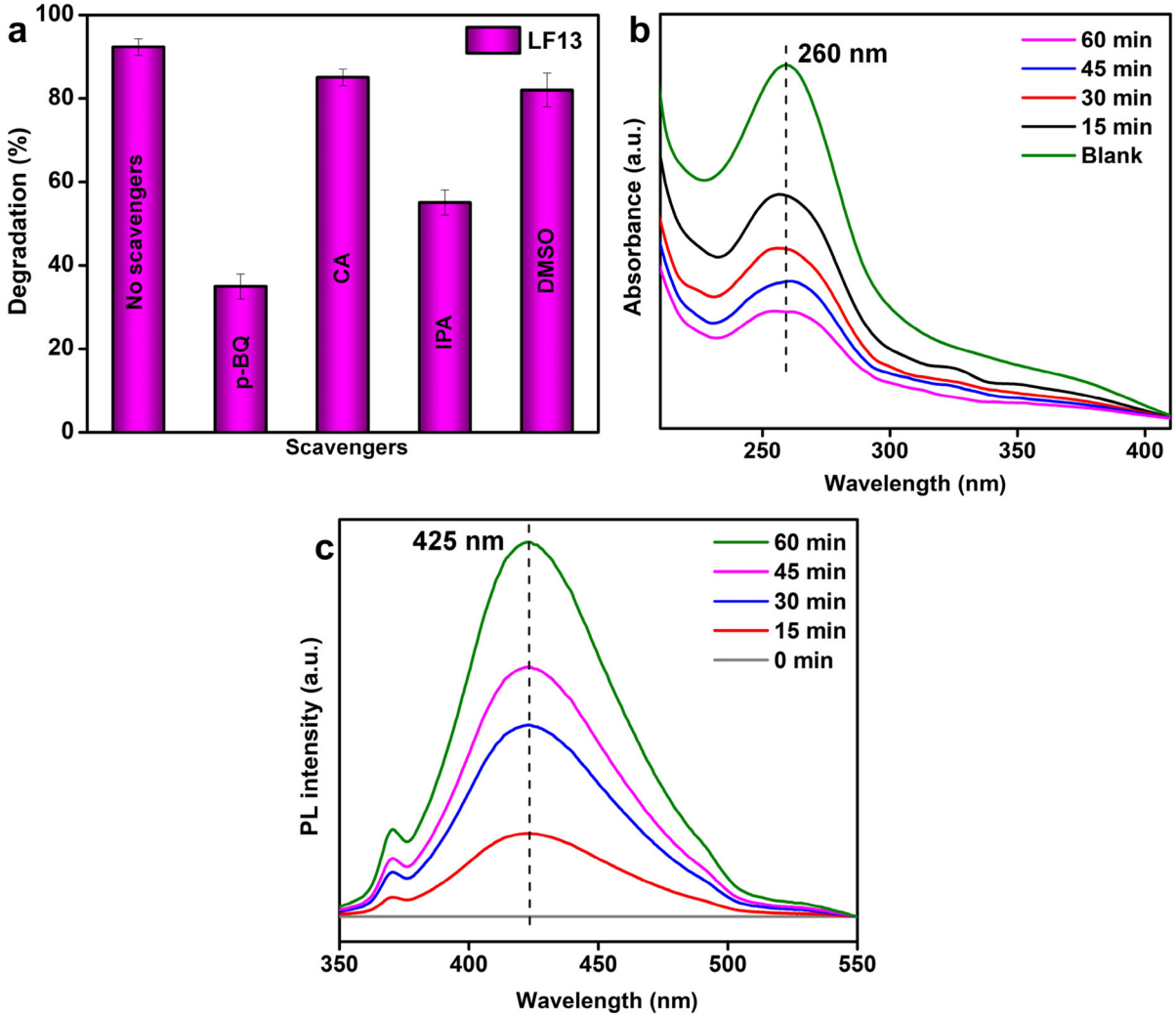

Fig. 6 The (a) scavenger test, (b) NBT test, and (c) TA-OH test plots carried out using the best nanocomposite LF13.

generated electrons, which enhances the availability of holes for water oxidation. However, the deposition of Ag/AgO on the catalyst surface in $AgNO_3$ obstructs light penetration and increases the solubility of the generated O_2 molecules. Additionally, the reusability plot (Fig. 8d) indicates a slight decline in the O_2 evolution rate with successive catalytic cycles, primarily due to catalyst loss during the recovery process. Table S3† presents a comparison of the OER performances reported for different catalysts.

3. Origin of the improved catalytic activity

The catalytic activity observed for the designed catalyst (pristine as well as binary heterostructure) can be attributed to many inherent characteristic features. To reveal the origin of the improved activity of the catalysts, the separation and migration of photogenerated charges, along with the S-P-F mechanism, were systematically explored. Besides, light absorbance, separation and migration of photogenerated excitons are crucial factors affecting photocatalytic activity.[8] To study the spatial separation of photoexcited charge carriers, researchers use photoluminescence (PL) emission spectra, where lower steady-state PL intensity indicates a lower recombination rate of photogenerated charges (by immediate quenching of the generated electrons), corresponding to higher photocatalytic activity (inversely proportional to the PL peak intensity). The PL spectra (at λ_{ex} = 375 nm, Fig. 9a) depicted an intense peak at 466 nm, responsible for the direct radiative charge carrier recombination occurring within the material. In contrast, the peak around 450 nm is ascribed to the transition of the electrons from the CB to the sub-VB and VB associated with all the samples.[8] Upon coupling FeOOH with LFO, similar PL peaks are observed for the composites but with reduced intensity, with LF13 having the lowest intensity, which exhibits the highest charge carrier separation. This

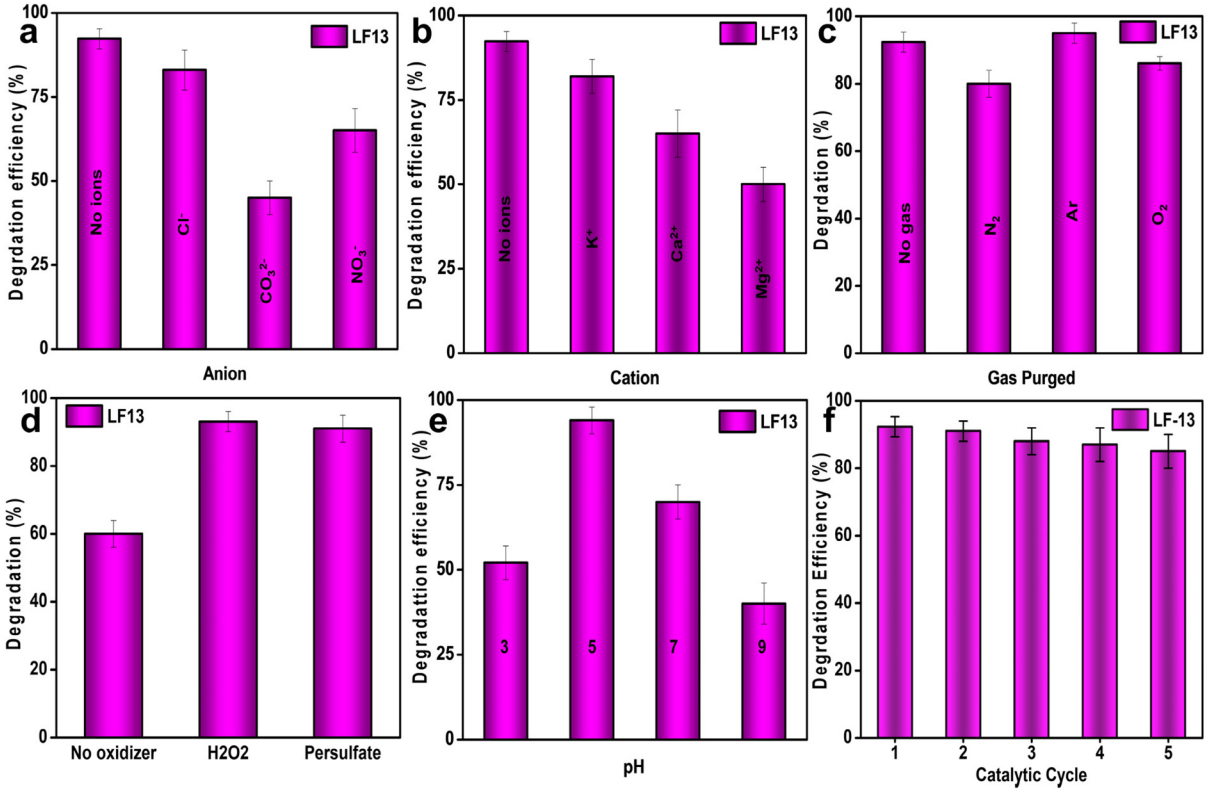

Fig. 7 Plots of OFL degradation subjected to various operational parameter tests using LF13: (a) anion test, (b) cation test, (c) gas sparged, (d) oxidant added, (e) pH variation, and (f) reusability test.

indicates that the presence of FeOOH in the LFO matrix efficaciously reduces the excessive charge carrier recombination, easing the formation of a close radiative pathway *via* the formation of an n–n junction. As a result, efficient charge transfer occurs due to the creation of a built-in electric field within the composite material. Besides, the rates of recombination are also governed by the existence of a heterojunction interface, trapped defects, and interparticle diffusion distance.[38]

Moreover, to attest the greater lifetime of excitons of LF13, time-resolved photoluminescence (TRPL) assessment was employed, and the respective fluorescence decay curves are fitted using biexponential decay functions represented in eqn (4), depicted in Fig. 9b.[55]

$$R(t) = A_1 \exp\{-t/\tau_1\} + A_2 \exp\{-t/\tau_2\} \quad (4)$$

where R, A, t, and τ represent normalized emission intensity, amplitude, time after pulsed laser excitation, and exciton lifetime (τ_1 = short lifetime, τ_2 = long lifetime) of the individual components, respectively. τ_1 and τ_2 represents the radiative and non-radiative relaxation processes of photo excitons, respectively. The τ_{avg} (average lifetime) was evaluated using the following equation:

$$\tau_{avg} = \frac{A_1\tau_1^2 + A_2\tau_2^2}{A_1\tau_1 + A_2\tau_2}\ \text{ns} \quad (5)$$

The calculated average lifetime of LF13 is 0.77 ns, which is higher than pristine LFO (0.14 ns) and FeOOH (0.124 ns). This indicates improved exciton separation and charge transfer within the binary hybrid material owing to the incorporation of FeOOH, resulting in enhanced catalytic activity.

The separation and transfer of photoproduced exciton were examined using an electrochemical impedance spectroscopy (EIS) study under simulated light (300 W) and zero bias voltage. The Nyquist plot reveals a straight line in the low-frequency region and a semicircle in the high-frequency region, collectively representing the system's charge transfer resistance. The arc radius observed in the Nyquist plot provides crucial insights into charge transfer resistance, charge separation efficiency, and the photocatalyst's conductivity. In Fig. 9c, the composite material exhibits the smallest semicircle radius, signifying lower charge transfer resistance, improved conductivity, and more efficient electron flow at the electrode–electrolyte interface. This behavior is attributed to the robust interfacial junction formed between LFO and FeOOH, which greatly enhances the overall performance of the hybrid system.

In the case of the linear sweep voltammetry (LSV) results, both LFO and FeOOH exhibited photocurrent response of the anodic type which points out the n-type characteristic of the

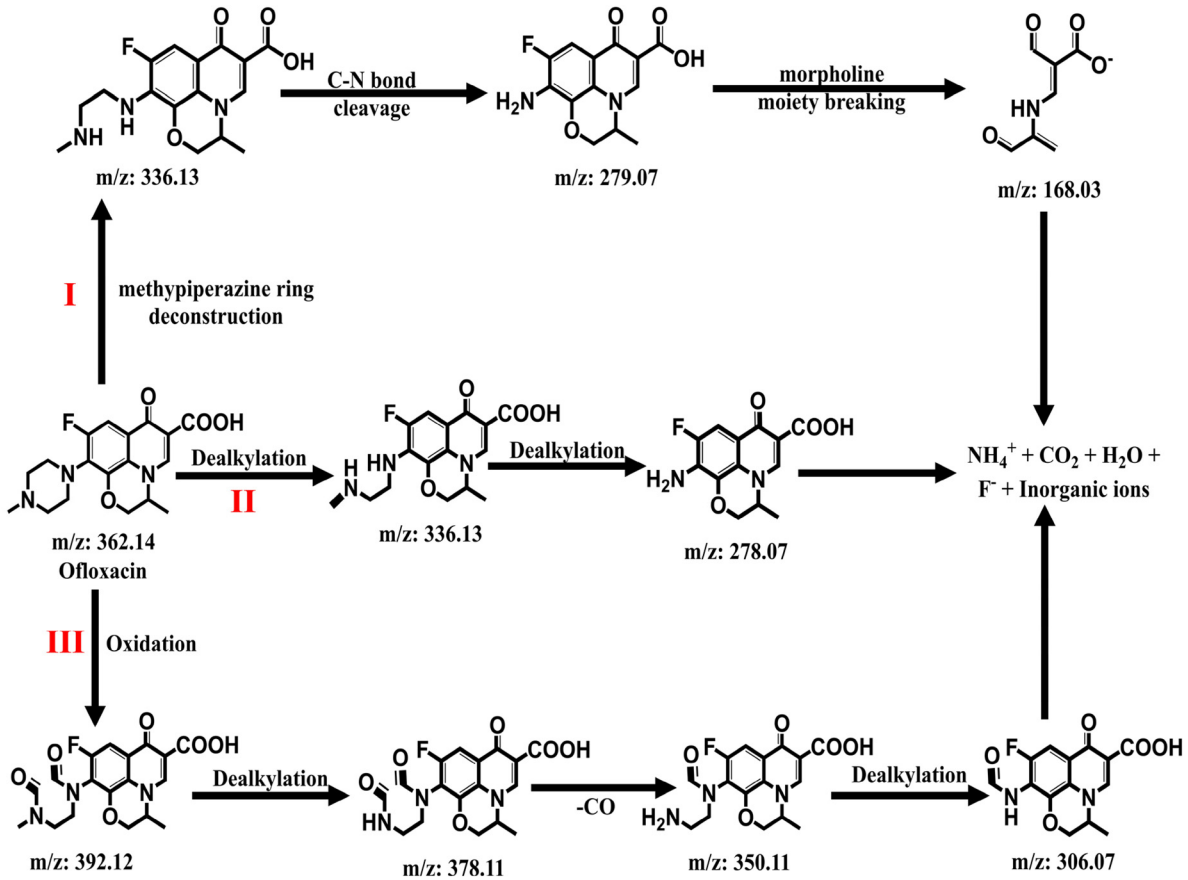

Scheme 2 The OFL degradation pathway using LF13 as the sono-photo-Fenton catalyst, thoroughly verified using the LC-MS study.

material. The recorded photocurrent responses (Fig. 9d) for LFO, FeOOH, and LF13 are 38, 150 and 631 μA cm^{-2}, respectively, which indicates the presence/availability of charge carriers. The photocurrent observations and the steadiness of pristine LFO, FeOOH, and LF-13 nanocomposites were analyzed using the transient photocurrent study. The optimized LF-13 catalyst exhibits a higher current density compared with bare material, which reveals the efficient charge divergence ability of the nanocomposite. The transient photocurrent (TPC) plot as depicted in Fig. 9e, suggests the highest photocurrent density for the LF13 composite compared with the neat and other composite variations, indicating an enhanced lifetime of charge carriers. Hence, it is evident that the presence of FeOOH efficiently suppresses the exciton pair recombination by trapping or transporting them to the LFO/FeOOH interfaces through the developed electric field.

Based on the above outcomes and discussions and the probable band offset at the interface of pristine materials in LF13 nanocomposite (Scheme S2†), we present a plausible mechanism that proves the reaction pathway to be reasonable towards the observed catalytic activity. LFO, when combined with FeOOH and subjected to photo and US irradiation, undergoes different reactions in two distinct phases, *i.e.*, the solid phase and the solution phase. The solid phase involves the photocatalytic reactions, whereas the solution phase involves the sono-Fenton and photo-Fenton reactions only, occurring simultaneously. Also, we mention the presence of both *ex situ* and *in situ* Fenton reactions that aid in achieving the desired degradation results. Besides, the photocatalysis reaction involved in the solid phase can probably follow two mechanistic pathways: type II and S-scheme.

Upon introducing FeOOH into the LFO matrix, a type II (staggered) heterostructure forms due to both pristine materials' broad light-harvesting range (as evident from the UV-DRS study). The band structure examination suggested that both LFO and FeOOH possess appropriate VB and CB positions suitable for transmitting e^- and h^+. When the two SCs come in close contact, e^- transmission is propelled from its higher (CB_{LFO}) to lower (CB_{FeOOH}) concentration region owing to the difference in the Fermi energy (E_f). Similarly, the transmission of h^+s occurs from VB_{FeOOH} (higher) to VB_{LFO} (lower) following the concentration gradient. Hence, for photocatalytic reactions, CB_{FeOOH} and VB_{LFO} serve as ideal e^- and h^+ centers, respectively. Although the band structure satisfies the type II arrangement, the heterojunction also comes with its demerits. Thermodynamically, enhanced charge separation in a type II arrangement reduces redox capability, which is unfavorable for photocatalytic reactions. Also, dynamic inter electron (CB_{LFO})

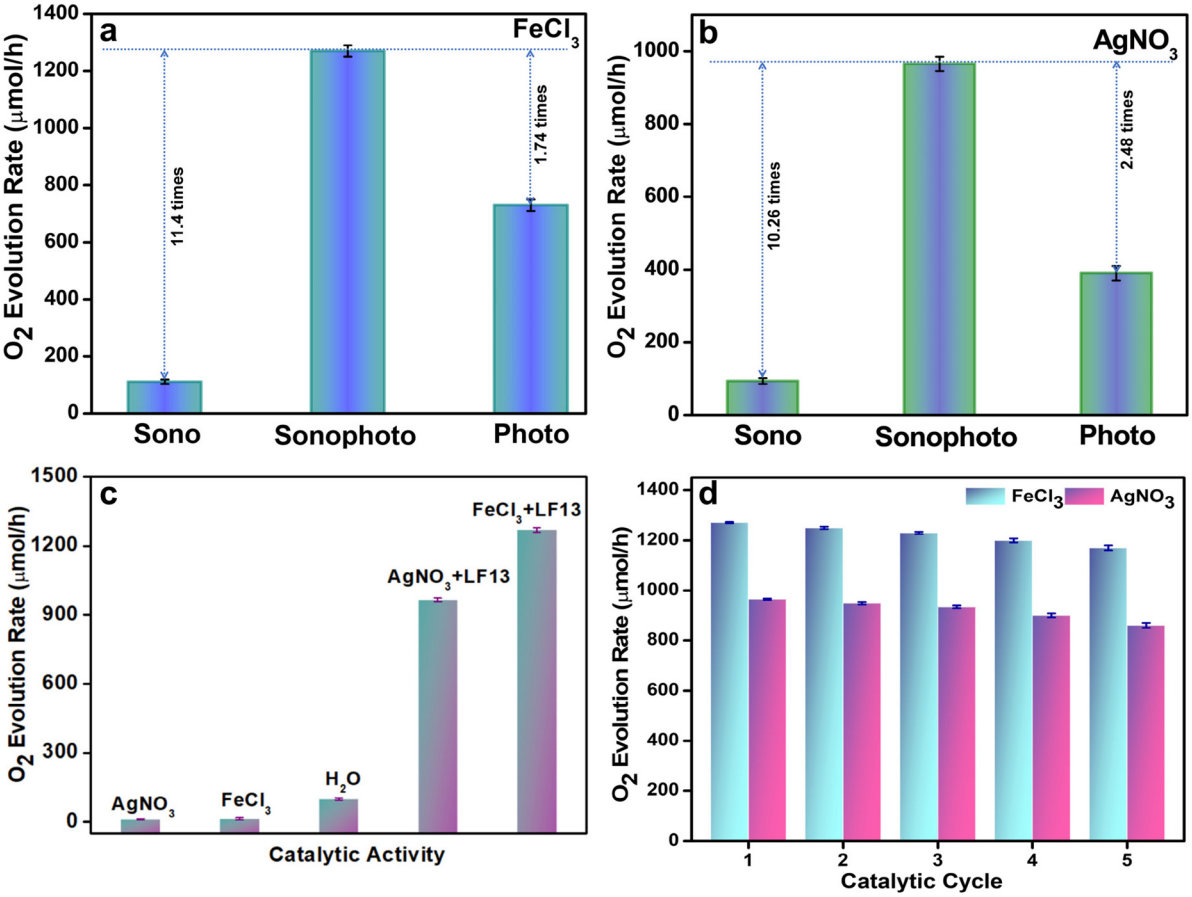

Fig. 8 O_2 evolution rate over LF13 in the presence of different sacrificial agents: (a) $FeCl_3$, (b) $AgNO_3$, (c) comparative plot, and (d) reusability plot.

and inter hole (VB_{LFO}) repulsions hinder the smooth flow of charges. Additionally, electrostatic attraction between e^- and h^+ within each photocatalyst further obstructs exciton movement. Thus, the traditional type-II heterojunction remains inefficient towards exciton separation and does not help achieve the desired results corresponding to the redox performance, necessitating reassessment.

Looking at the W, VB, CB, and overall energy band structure of the individual semiconductors, along with their respective band potential corresponding to specific applications or reactive species generation (based on feasibility), the proposed sono-photo-Fenton reaction pathway involves the integration of the photocatalytic S-scheme heterojunction mechanistic charge flow pathway along with the US cavitation effect in the presence of a Fenton reaction environment, as depicted in Scheme 3. Pristine FeOOH exhibits a more significant work function compared with LFO, indicating that the E_f of LFO is greater than that of FeOOH. When the two SCs come in close contact, free electrons spontaneously rearrange, and electrons flow from LFO to FeOOH (lower to higher ϕ) until their Fermi levels equalize at the interface. This e^- transfer results in LFO becoming positively charged due to the loss of electrons, forming an electron depletion region, while the interface of FeOOH becomes negatively charged due to electron accumulation. This establishes a built-in electric field (BE) known as the space charge region, directed from LFO to FeOOH, which later enhances the propagation of photogenerated electrons from the CB_{FeOOH} to the VB_{LFO}. By virtue of this region, the LFO and FeOOH energy bands at the interface undergo upward and downward bending, respectively, enabling the development of a potential barrier at a noted height and further preventing the Type II transfer. This internal electric field balances the Fermi levels of FeOOH and LFO, preventing further electron transfer across the interface. Upon light irradiation, electrons are stimulated from the VB to the CB in both LFO and FeOOH. The internal electric field, band bending, and Coulomb interactions cause the photoexcited electrons in CB_{FeOOH} to migrate to the VB_{LFO} and recombine with h^+s. This process leads to the retention of highly reductive electrons in the CB_{LFO} and highly oxidative h^+s in the VB_{FeOOH}. This facilitates the efficient transfer of photogenerated electrons from the LFO/FeOOH (LF13) to the photocatalyst surface, which acts as an electron sink due to weak van der Waals forces that promote its adsorption onto the photocatalyst surface. Thus, the S-scheme heterojunction pathway offers advantages for separating photogenerated e^-/h^+ besides preserving high redox potential. The higher-reduction-potential electrons in LFO react with dissolved O_2 to form $^{\bullet}O_2^-$, which

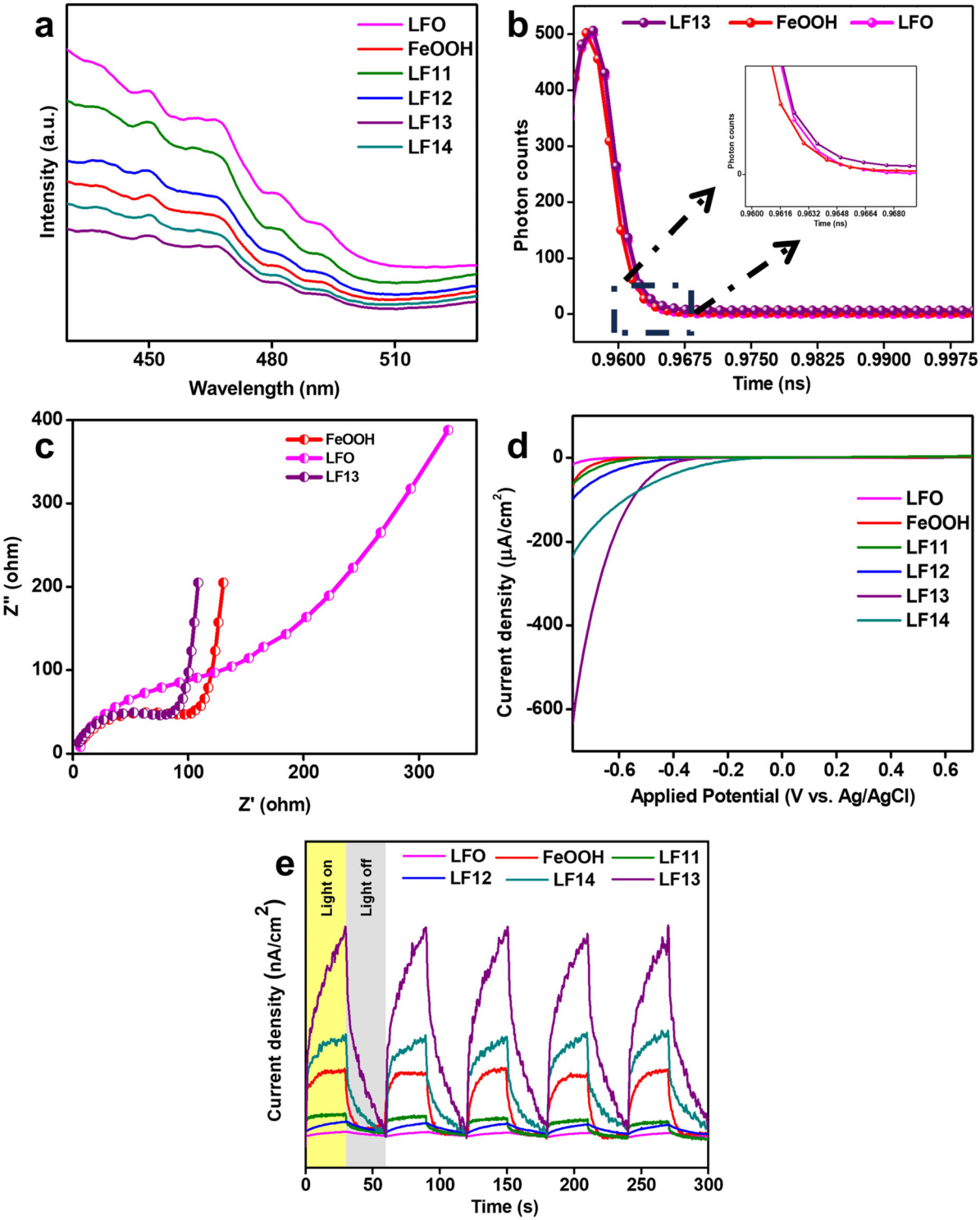

Fig. 9 The (a and b) PL and TRPL spectra excited at 375 nm; (c) electrochemical impedance spectroscopy (EIS) spectra, (d) linear sweep voltammetry (LSV) plot, and (e) transient photocurrent (TPC) plot for the pristine and nanocomposite materials.

produces H_2O_2 (primary reaction), resulting in further decomposition which leads to the generation of $^{\bullet}OH$, while the strong oxidizing h^+s in FeOOH oxidize H_2O to generate $^{\bullet}OH$ (not so contributing reaction), as depicted in eqn (6)–(14). This mechanism confirms that the S-scheme heterojunction is beneficial for efficient e^-/h^+ separation, thereby enhancing photocatalytic performance.

Besides the reactions in the solid phase, the solution phase reactions significantly add to the ofloxacin degradation performance, represented in eqn (15)–(25). These reactions

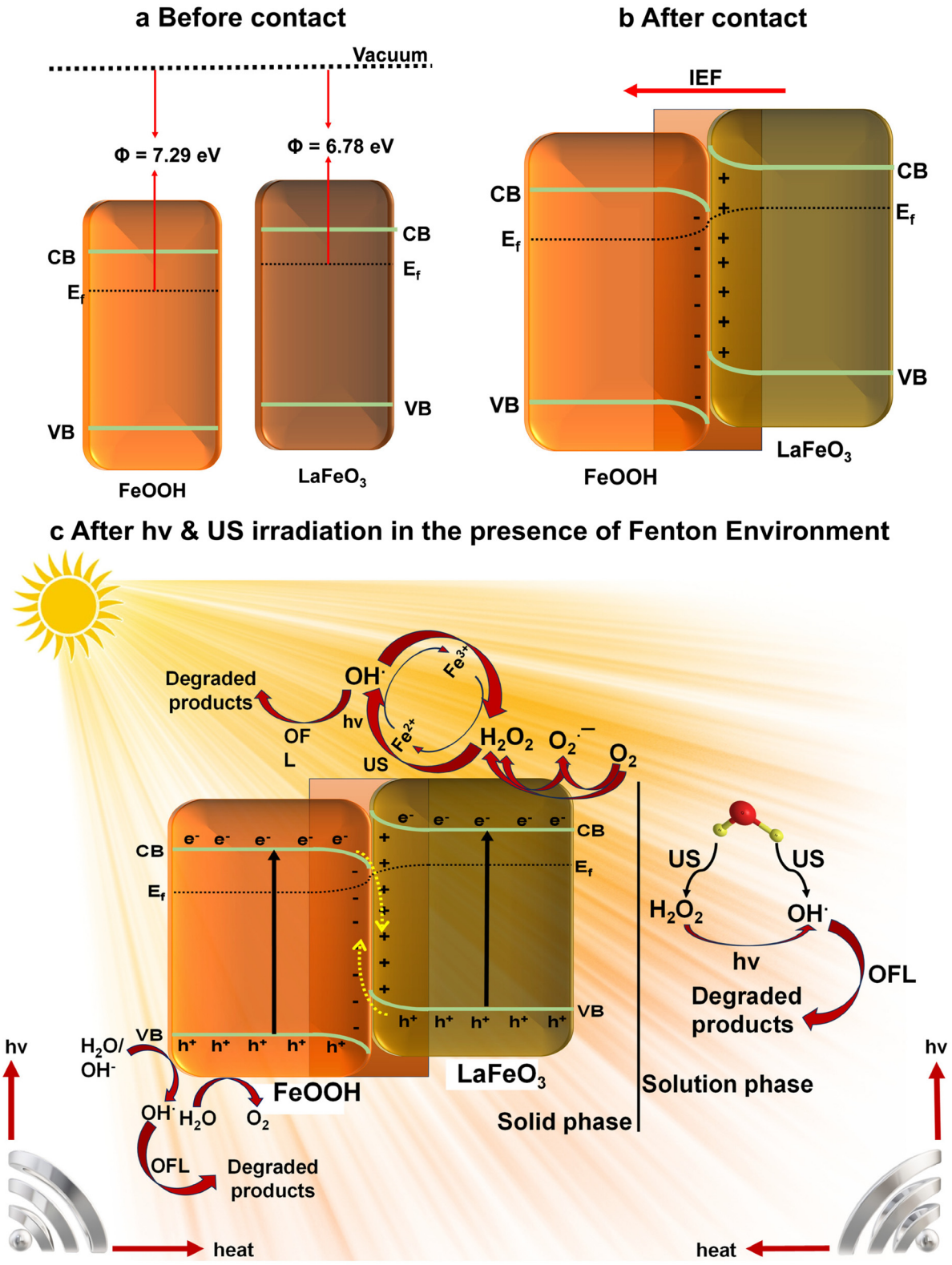

Scheme 3 The pathway involved in the sono-photo-Fenton ofloxacin degradation and the OER.

involve *in situ* and *ex situ* SF as well as PF reactions. Here, we consider that the generation of *in situ* H_2O_2 plays a crucial role in the degradation mechanism along with the external addition of H_2O_2 (which takes part in the *ex situ* reaction). When US waves are applied to the reaction system, sonoluminescence, hot spot, and cavitation effects are the major players

responsible for the SF performance. Through the cavitation effect during sonoluminescence, US irradiation generates visible light with a relatively broad wavelength range. Also, the "hot spot" phenomenon involves the generation of heat through the US cavitation in an aqueous medium capable of decomposing water molecules to $^{\bullet}OH$, $^{\bullet}HO_2$, and H_2O_2. The resulting H_2O_2 molecules can be converted into $^{\bullet}OH$ radicals *in situ* and *ex situ* through further US irradiation. Moreover, in a Fenton environment, an optimum amount of Fe salt is necessary for a Fenton reaction, where the complete conversion of Fe^{2+} to Fe^{3+} ends the reaction. To keep the reaction going, Fe^{2+} ions must be periodically added, which is compensated by the presence of the LFO@FeOOH heterojunction, depicted in eqn (26)–(28). Besides, a sono-appropriate SC reacts with electrons to generate additional free radicals. The heat energy from the "hot spots" can also excite the catalyst to form e^-–h^+ pairs, thereby generating even more reactive oxidizing species. Hence, the convincing sono-photo-Fenton mechanism can be summarised in the following equations.

Reactions in the solid phase:

$$\text{LF13} + h\nu \rightarrow h^+(\text{VB}) + e^-(\text{CB}) \quad (6)$$

$$\text{LF13}+))))) \rightarrow {h_{VB}}^+ + {e_{CB}}^- \quad (7)$$

At VB_{FeOOH}:

$$h^+ + H_2O \rightarrow {OH^{\bullet}}_{ads} + H^+ \quad (8)$$

$$h^+ + {OH_{ads}}^- \rightarrow {OH^{\bullet}}_{ads} \quad (9)$$

At CB_{LFO}:

$$e^- + O_2 \rightarrow {O_2}^{\bullet -} \quad (10)$$

$$e^- + {O_2}^{\bullet -} + 2H^+ \rightarrow H_2O_2 \quad (11)$$

$${O_2}^{\bullet -} + {O_2}^{\bullet -} + 2H^+ \rightarrow H_2O_2 + O_2 \quad (12)$$

$${O_2}^{\bullet -} + H_2O \rightarrow {OH_{ads}}^{\bullet} + OH^- \quad (13)$$

$${O_2}^{\bullet -} + H_2O_2 \rightarrow {OH_{ads}}^{\bullet} + OH^- + O_2 \quad (14)$$

Reactions in the solution phase:

By $h\nu$ irradiation:

$$Fe^{3+} + H_2O + h\nu \rightarrow Fe^{2+} + OH^{\bullet} + H^+ \quad (15)$$

$$OH^{\bullet} + {HO_2}^{\bullet} \rightarrow H_2O + O_2 \quad (16)$$

$${HO_2}^{\bullet} + {HO_2}^{\bullet} \rightarrow H_2O_2 + O_2 \quad (17)$$

$$H_2O_2 + h\nu \rightarrow 2OH^{\bullet} \quad (18)$$

By US:

$$O_2+))) \rightarrow 2O^{\bullet} \quad (19)$$

$$H_2O + O^{\bullet} \rightarrow 2OH^{\bullet} \quad (20)$$

$$Fe^{2+} + OH^{\bullet} \rightarrow Fe^{3+} + OH^- \quad (21)$$

$$OH^{\bullet} + OH^{\bullet} \rightarrow H_2O_2 \quad (22)$$

$$H^{\bullet} + OH^{\bullet} \rightarrow H_2O \quad (23)$$

$$H^{\bullet} + H_2O_2 \rightarrow OH^{\bullet} + H_2O \quad (24)$$

$$Fe^{3+} + H^{\bullet} \rightarrow Fe^{2+} + H^+ \quad (25)$$

Reactions induced by the Fenton environment:

$$Fe^{2+} + H_2O_2 + H^+ \rightarrow Fe^{3+} + OH^{\bullet} + H_2O \quad (\text{in acidic medium}) \quad (26)$$

$$Fe^{2+} + OH^{\bullet} \rightarrow Fe^{3+} + OH^- \quad (27)$$

$$OH^{\bullet} + OH^{\bullet} \rightarrow H_2O_2 \quad (28)$$

Ofloxacin degradation:

$$\text{Ofloxacin} + OH^{\bullet}\,(\text{ROS}) \rightarrow H_2O + CO_2 + \text{other degradation products} \quad (29)$$

The novel application of an S-scheme heterojunction into an S-P-FR system synergistically enhances the exciton pair separation, redox ability, and ROS generation. Unlike the traditional PF and SF systems, the S-scheme mechanism selectively transfers high-energy electrons and holes while discarding low-energy carriers, improving catalytic efficiency. The US cavitation effect further boosts $^{\bullet}OH$ radical production, catalyst dispersion, and charge dynamics. This approach helps in overcoming pH limitations, enhancing visible-light absorption, reducing Fe-leaching through sustainable Fe^{2+} regeneration, and enhancing the catalyst stability. Compared with previous studies, this method uniquely integrates sonocatalysis, photocatalysis, and Fenton chemistry, enabling a highly efficient and sustainable AOP for antibiotic degradation.

The OER mechanism in the presence of $FeCl_3$ as a sacrificial agent involves the interaction between Fe^{3+} ions and photogenerated charge carriers, facilitating enhanced charge separation and improved oxygen generation. In the presence of $FeCl_3$, electron scavenging by Fe^{3+} minimizes electron–hole recombination, while increased hole availability accelerates water oxidation to O_2, and cyclic regeneration of Fe^{3+} sustains the catalytic process, enhancing OER efficiency. The combination of photoexcitation, piezoelectric polarization, and Fe^{3+} scavenging significantly improves the O_2 evolution rate. Here is a stepwise breakdown of the mechanism:

$$\text{LF13} + h\nu+))) \rightarrow {e_{CB}}^- + {h_{VB}}^+ \quad (30)$$

$$2H_2O + 4h^+ \rightarrow O_2 + 4h^+\ (\text{aq.}) \quad (31)$$

$$Fe^{3+} + h^+ \rightarrow Fe^{3+} \quad (32)$$

$$Fe^{3+} + H_2O \rightarrow Fe^{2+} + O_2 \quad (33)$$

$$\text{LF13} + h\nu+))) \rightarrow {e_{VB}}^- + {h_{VB}}^+ \quad (34)$$

$$h^+ + Ag^+ \rightarrow Ag^{2+} \quad (35)$$

$$Ag^{2+} + H_2O \rightarrow Ag_2O_2 + 4h^+\ (\text{aq.}) \quad (36)$$

$$Ag_2O_2 + 2h^+ \rightarrow 2Ag^+ + O_2 \quad (37)$$

Hence, the accelerated catalytic performance of LF13 semiconductor is ascribed to the following reasons:

i. *The construction of FeOOH@LaFeO$_3$ binary heterojunction*: the intimate interfacial interaction between FeOOH and $LaFeO_3$ facilitates the transfer of exciton pairs, reducing charge recombination and increasing the availability of active species for pollutant degradation. Also, the anchoring of FeOOH on $LaFeO_3$ increases the surface area and availability of catalytic sites, thereby augmenting the interactions between the photocatalyst and pollutant.

ii. *Presence of ample surface O$_V$s*: O_Vs behave as shallow electron trap states, inhibiting the surface and bulk recombination rate as well as acting as electron donors, hiking charge carrier density. O_V enhances the light absorption ability by the introduction of mid-gap states. O_Vs also facilitate H_2O adsorption and dissociation over the surface, which is critical in water splitting reactions.

iii. *S-scheme charge transfer dynamics*: S-scheme pathway facilitates a selective recombination of low-energy excitons at the heterointerface, preserving high-energy e^-s and high-energy h^+s in the reduction-side (CB) and oxidation-side (VB) of the semiconductor. In the present system, visible light irradiation stimulates both the catalysts and helps in the formation of exciton pairs. The photogenerated electrons in CB_{FeOOH} and the holes in VB_{LaFeO_3}, which have comparatively lower redox potentials, recombine at the interface. This selective recombination method preserves electrons with considerable reducing capacity in LFO and holes with high oxidizing potential in FeOOH, which are then utilized for redox reactions, OFL degradation, and oxygen evolution.

iv. *Ultrasonic irradiation generated acoustic cavitation*: ultrasonic cavitation results in the formation of localized regions characterized by extremely high temperatures and pressures, promoting the production of ROS such as $^{\bullet}OH$ and H_2O_2. Also, ultrasound enhances mass transfer and accelerates the Fe^{2+}/Fe^{3+} redox cycle, improving the overall catalytic activity.

v. *Fenton reaction*: the Fenton reaction is crucial in enhancing photocatalytic activity by facilitating the production of highly reactive $^{\bullet}OH$, which are essential oxidative species for the fast destruction of organic contaminants. In this reaction, Fe^{2+} ions interact with H_2O_2 to generate $^{\bullet}OH$ radicals and Fe^{3+}. Owing to the abundant Fe-sites, FeOOH acts as an efficient Fenton catalyst, simultaneously oscillating between Fe^{2+} and Fe^{3+} oxidation states due to photogenerated electrons and ultrasonic cavitation. Moreover, the sono-assisted environment enhances the breakdown of H_2O_2 and optimizes the dispersion and reactivity of intermediates.

vi. *Synergism among Ov, binary heterojunction, light irradiation ultrasonication, and S-scheme charge transfer pathway*: upon light irradiation, both of the pristine materials generate excitons; however, the S-scheme mechanism facilitates the recombination of low-energy electrons-holes at the interface selectively, without disturbing high-energy charge carriers having superior redox ability for reactions. The process is further supplemented by ultrasonication, inducing acoustic cavitation, creating shockwaves, micro-jets, and localized hot spots, which augment H_2O_2 activation and increase surface accessibility. This collaborative interaction guarantees effective charge separation and increased ROS production while promoting OER during water splitting.

4. Conclusions

This is the first study showing the successful design and introduction of a robust binary $LaFeO_3$@FeOOH heterostructure following a facile two-step fabrication strategy to explore the integration of S-scheme charge transfer with ultrasonic-assisted photo-Fenton catalysis, achieving efficient degradation of antibiotic (OFL) and water splitting. The synergistic effects of oxygen vacancies, built-in electric fields, and cavitation-driven ROS generation enable superior charge separation and redox performance toward water treatment to prevent antibiotic resistance of OFL. The fabricated catalyst exhibited an efficient OFL degradation of 92.3% in 1 h *via* the MOA method and an OER of 1270 μmol h^{-1} through water splitting under the influence of both ultrasonic vibration and simulated solar light *via* the MOA method. The presence of O_V triggers fast charge migration and facilitates more active sites for surface catalytic reactions. This work presents a sustainable approach for environmental cleanup and energy applications, serving as a model for next-generation multifunctional catalysts.

Data availability

The submitted research article synthesizes and discusses data that have not been published elsewhere. The data supporting this article have been included as part of the ESI.†

Conflicts of interest

The authors declare no competing financial interest.

Acknowledgements

The authors deeply appreciate Siksha 'O' Anusandhan (Deemed to be University) for providing the essential resources and financial assistance needed to conduct this extensive research project. Ms Newmoon Priyadarshini acknowledges to CSIR, India for awarding CSIR-SRF (appl. no.: 122-3839-9690/2K23/1). The authors are also thankful to Dr Raghavender Medishetty, Indian Institute of Technology, Bhilai, for supporting the Raman characterizations. The authors are immensely obliged to Ms Priyanka Priyadarshini for the technical and friendly support rendered throughout the drafting of the manuscript.

References

1 M. Farghali, A. I. Osman, I. M. A. Mohamed, Z. Chen, L. Chen, I. Ihara, P. S. Yap and D. W. Rooney, Strategies to save energy in the context of the energy crisis: a review, *Environ. Chem. Lett.*, 2023, 1–37, DOI: **10.1007/s10311-023-01591-5**.

2 K. H. Ng, S. Y. Lai, C. K. Cheng, Y. W. Cheng and C. C. Chong, Photocatalytic water splitting for solving energy crisis: Myth, Fact or Busted?, *Chem. Eng. J.*, 2021, **417**, 128847.

3 E. Pierrat, A. Laurent, M. Dorber, M. Rygaard, F. Verones and M. Hauschild, Advancing water footprint assessments: Combining the impacts of water pollution and scarcity, *Sci. Total Environ.*, 2023, **870**, 161910.

4 G. G. Bessegato, T. T. Guaraldo, J. F. de Brito, M. F. Brugnera and M. V. B. Zanoni, Achievements and Trends in Photoelectrocatalysis: from Environmental to Energy Applications, *Electrocatalysis*, 2015, **6**, 415–441.

5 R. Changotra, A. K. Ray and Q. He, Establishing a water-to-energy platform via dual-functional photocatalytic and photoelectrocatalytic systems: A comparative and perspective review, *Adv. Colloid Interface Sci.*, 2022, **309**, 102793.

6 J. Li, J. Ren, S. Li, G. Li, M. M.-J. Li, R. Li, Y. S. Kang, X. Zou, Y. Luo, B. Liu and Y. Zhao, Potential industrial applications of photo/electrocatalysis: Recent progress and future challenges, *Green Energy Environ.*, 2024, **9**, 859–876.

7 L. Reggiane de Carvalho Costa, K. Guerra Pacheco Nunes and L. Amaral Féris, Ultrasound as an Advanced Oxidative Process: A Review on Treating Pharmaceutical Compounds, *Chem. Eng. Technol.*, 2021, **44**, 1744–1758.

8 F. Li, L. Cheng, J. Fan and Q. Xiang, Steering the behavior of photogenerated carriers in semiconductor photocatalysts: a new insight and perspective, *J. Mater. Chem. A*, 2021, **9**, 23765–23782.

9 M. Moradi, A. Elahinia, Y. Vasseghian, E.-N. Dragoi, F. Omidi and A. Mousavi Khaneghah, A review on pollutants removal by Sono-photo -Fenton processes, *J. Environ. Chem. Eng.*, 2020, **8**, 104330.

10 A. Mishra, N. Priyadarshini, S. Mansingh and K. Parida, Recent advancement in LaFeO(3)-mediated systems towards photocatalytic and photoelectrocatalytic hydrogen evolution reaction: A comprehensive review, *Adv. Colloid Interface Sci.*, 2024, **333**, 103300.

11 S. Patnaik, A. Behera and K. Parida, A review on g-C3N4/graphene nanocomposites: multifunctional roles of graphene in the nanohybrid photocatalyst toward photocatalytic applications, *Catal. Sci. Technol.*, 2021, **11**, 6018–6040.

12 P. Prabha Sarangi, D. Prava Sahoo, U. Aparajita Mohanty, S. Nayak and K. Parida, Recent Advancement in Quantum Dot Modified Layered Double Hydroxide towards Photocatalytic, Electrocatalytic, and Photoelectrochemical Applications, *ChemCatChem*, 2024, **16**, e202301533.

13 P. Behera, S. Subudhi, S. P. Tripathy and K. Parida, MOF derived nano-materials: A recent progress in strategic fabrication, characterization and mechanistic insight towards divergent photocatalytic applications, *Coord. Chem. Rev.*, 2022, **456**, 214392.

14 B. P. Mishra, S. Das, L. Biswal, L. Acharya, J. Sahu and K. Parida, MXene Schottky Functionalized Z-scheme Ternary Heterostructure for Enhanced Photocatalytic H_2O_2 Production and H2 Evolution, *J. Phys. Chem. C*, 2024, **128**, 1921–1935.

15 J. Sahu, D. Prusty, S. Mansingh and K. Parida, A review on alloyed quantum dots and their applications as photocatalysts, *Int. J. Hydrogen Energy*, 2023, **48**, 29097–29118.

16 G. Swain, S. Sultana and K. Parida, One-Pot-Architectured Au-Nanodot-Promoted MoS(2)/ZnIn(2)S(4): A Novel p-n Heterojunction Photocatalyst for Enhanced Hydrogen Production and Phenol Degradation, *Inorg. Chem.*, 2019, **58**, 9941–9955.

17 S. Subudhi, S. P. Tripathy and K. Parida, Metal oxide integrated metal organic frameworks (MO@MOF): rational design, fabrication strategy, characterization and emerging photocatalytic applications, *Inorg. Chem. Front.*, 2021, **8**, 1619–1636.

18 C. Moure and O. Peña, Recent advances in perovskites: Processing and properties, *Prog. Solid State Chem.*, 2015, **43**, 123–148.

19 K. Wang, C. Han, Z. Shao, J. Qiu, S. Wang and S. Liu, Perovskite Oxide Catalysts for Advanced Oxidation Reactions, *Adv. Funct. Mater.*, 2021, **31**, 2102089.

20 L. Hao, H. Huang, Y. Zhang and T. Ma, Oxygen Vacant Semiconductor Photocatalysts, *Adv. Funct. Mater.*, 2021, **31**, 2100919.

21 Q. Feng, J. Zhou, W. Luo, L. Ding and W. Cai, Photo-Fenton removal of tetracycline hydrochloride using LaFeO(3) as a persulfate activator under visible light, *Ecotoxicol. Environ. Saf.*, 2020, **198**, 110661.

22 S. G. Babu, P. Aparna, G. Satishkumar, M. Ashokkumar and B. Neppolian, Ultrasound-assisted mineralization of organic contaminants using a recyclable LaFeO(3) and Fe (3+)/persulfate Fenton-like system, *Ultrason. Sonochem.*, 2017, **34**, 924–930.

23 K. M. Parida, A. Nashim and S. K. Mahanta, Visible-light driven Gd2Ti2O7/GdCrO3 composite for hydrogen evolution, *Dalton Trans.*, 2011, **40**, 12839–12845.

24 T. M. Khedr, K. Wang, D. Kowalski, S. M. El-Sheikh, H. M. Abdeldayem, B. Ohtani and E. Kowalska, Bi2WO6–based Z-scheme photocatalysts: Principles, mechanisms and photocatalytic applications, *J. Environ. Chem. Eng.*, 2022, **10**, 107838.

25 A. S. Basaleh, T. M. Khedr and R. M. Mohamed, Synergistic augmentation and rapid elimination of ciprofloxacin using a novel mesoporous nickel sulfide-adorned bismuth tungstate S-scheme heterojunction, *Mater. Today Sustainability*, 2024, **26**, 100762.

26 M. Mokhtar, A. S. Basaleh, R. M. Mohamed and T. M. Khedr, Novel MnCo2O4/YVO4 heterostructure for promoting photocatalytic oxidative desulfurization of thio-

phene under visible light, *Ceram. Int.*, 2024, **50**, 41145–41155.

27 S. Z. Alsheheri and T. M. Khedr, Green fabrication of aniline over mesoporous NiS/YVO4 S-type heterostructure photocatalyst under visible light exposure, *Mater. Sci. Semicond. Process.*, 2025, **186**, 109064.

28 Y. Li, Y. Wu, M. Yuan, H. Hao, Z. Lv, L. Xu and B. Wei, Operando spectroscopies unveil interfacial FeOOH induced highly reactive β-Ni(Fe)OOH for efficient oxygen evolution, *Appl. Catal., B*, 2022, **318**, 121825.

29 V. V. Strykanova, L. B. Gulina, V. P. Tolstoy, E. V. Tolstobrov, D. V. Danilov and I. Skvortsova, Synthesis of the FeOOH Microtubes with Inner Surface Modified by Ag Nanoparticles, *ACS Omega*, 2020, **5**, 15728–15733.

30 Q. Wang, R. Zhao, H. Li, S. Sun, Y. Sun, W. Gu, ... and X. Li, Oxygen vacancy-mediated Bi2WO6/FeOOH heterojunction for efficient photo-Fenton degradation antibiotics and synergistic sterilization, *Sep. Purif. Technol.*, 2025, **359**, 130546.

31 G. Ge, M. Liu, C. Liu, W. Zhou, D. Wang, L. Liu and J. Ye, Ultrathin FeOOH nanosheets as an efficient cocatalyst for photocatalytic water oxidation, *J. Mater. Chem. A*, 2019, **7**, 9222–9229.

32 K. Chu, F. Liu, J. Zhu, H. Fu, H. Zhu, Y. Zhu, Y. Zhang, F. Lai and T. Liu, A General Strategy to Boost Electrocatalytic Nitrogen Reduction on Perovskite Oxides via the Oxygen Vacancies Derived from A–Site Deficiency, *Adv. Energy Mater.*, 2021, **11**, 2003799.

33 M. K. Wang, P.-T. Yang, T.-J. Chuang, C. C. Ou and S. L. Wang, Crystallization between (100) Goethite and (001) Orientation of Hematite – A Review, *Clays Clay Miner.*, 2024, **71**, 242–251.

34 Z. Sadighi, J. Huang, L. Qin, S. Yao, J. Cui and J.-K. Kim, Positive role of oxygen vacancy in electrochemical performance of CoMn 2 O 4 cathodes for Li-O 2 batteries, *J. Power Sources*, 2017, **365**, 134–147.

35 S. Mansingh, S. Subudhi, S. Sultana, G. Swain and K. Parida, Cerium-Based Metal–Organic Framework Nanorods Nucleated on CeO_2 Nanosheets for Photocatalytic N2 Fixation and Water Oxidation, *ACS Appl. Nano Mater.*, 2021, **4**, 9635–9652.

36 G. H. M. Gomes, J. B. Gabriel, C. G. O. Bruziquesi, H. V. Victoria, K. Krambrock, L. C. A. Oliveira and N. D. S. Mohallem, The role of oxygen vacancies in TT-Nb2O5 nanoparticles for the photoconversion of glycerol into solketal, *Ceram. Int.*, 2023, **49**, 14719–14732.

37 S. M. Khetre, H. V. Jadhav and S. R. Bamane, Synthesis and characterization of nanocrystalline LaFeO3 by combustion route, *Rasayan J. Chem.*, 2010, **3**(1), 82–86.

38 N. Priyadarshini, S. Mansingh, K. K. Das, R. Garg, Sumit, K. Parida and K. Parida, Macroscopic Spontaneous Piezopolarization and Oxygen-Vacancy Coupled Robust NaNbO(3)/FeOOH Heterojunction for Pharmaceutical Drug Degradation and O(2) Evolution: Combined Experimental and Theoretical Study, *Inorg. Chem.*, 2024, **63**, 256–271.

39 B. G. Kim, J. Park, W. Choi, D. S. Han, J. Kim and H. Park, Electrocatalytic arsenite oxidation using iron oxyhydroxide polymorphs (α-, β-, and γ-FeOOH) in aqueous bicarbonate solution, *Appl. Catal., B*, 2021, **283**, 119608.

40 F. X. Xiao, Construction of highly ordered ZnO-TiO2 nanotube arrays (ZnO/TNTs) heterostructure for photocatalytic application, *ACS Appl. Mater. Interfaces*, 2012, **4**, 7055–7063.

41 S. Guan, H. Yang, X. Sun and T. Xian, Preparation and promising application of novel LaFeO3/BiOBr heterojunction photocatalysts for photocatalytic and photo-Fenton removal of dyes, *Opt. Mater.*, 2020, **100**, 109644.

42 Y. Jiang, Q. Lv, F. Xu, X. Sun and Y. Ding, Synthesis of TiO2/LaFeO3 composites for the photoelectrochemical hydrogen evolution, *J. Mater. Sci.*, 2021, **56**, 15188–15204.

43 S. Mansingh, D. Kandi, K. K. Das and K. Parida, A Mechanistic Approach on Oxygen Vacancy-Engineered CeO (2) Nanosheets Concocts over an Oyster Shell Manifesting Robust Photocatalytic Activity toward Water Oxidation, *ACS Omega*, 2020, **5**, 9789–9805.

44 Q. Liu, Z. You, S. J. Zeng and H. Guo, Infrared properties of Mg-doped LaFeO3 prepared by sol–gel method, *J. Sol-Gel Sci. Technol.*, 2016, **80**, 860–866.

45 J. Shi, Y. Chang, Y. Tang, X. Wang, X. Wang, X. Zhang and J. Cao, Hydrogenated LaFeO3 with oxygen vacancies for Enhanced Visible light photocatalytic performance, *Ceram. Int.*, 2020, **46**, 5315–5322.

46 G. Iervolino, V. Vaiano, D. Sannino, L. Rizzo and P. Ciambelli, Production of hydrogen from glucose by LaFeO 3 based photocatalytic process during water treatment, *Int. J. Hydrogen Energy*, 2016, **41**, 959–966.

47 M. Abou-Sekkina, M. El-Kersh and O. Shalma, Thermophysical properties of gamma-irradiated LaFeO 3 and YFeO 3 orthoferrites, *J. Radioanal. Nucl. Chem.*, 1999, **241**(1), 15–24.

48 *Porous materials: theory and its application for environmental remediation*, ed, J. C. Moreno-Piraján, L. Giraldo-Gutierrez and F. Gómez-Granados, Springer Nature, 2021.

49 R. Bardestani, G. S. Patience and S. Kaliaguine, Experimental methods in chemical engineering: specific surface area and pore size distribution measurements—BET, BJH, and DFT, *Canadian J. Chem. Eng.*, 2019, **97**, 2781–2791.

50 S. Acharya, D. K. Padhi and K. M. Parida, Visible light driven LaFeO3 nano sphere/RGO composite photocatalysts for efficient water decomposition reaction, *Catal. Today*, 2020, **353**, 220–231.

51 K. Wang, Z. Guan, X. Liang, S. Song, P. Lu, C. Zhao, L. Yue, Z. Zeng, Y. Wu and Y. He, Remarkably enhanced catalytic performance in CoO(x)/Bi(4)Ti(3)O(12) heterostructures for methyl orange degradation via piezocatalysis and piezo-photocatalysis, *Ultrason. Sonochem.*, 2023, **100**, 106616.

52 K. K. Das, U. A. Mohanty, R. Mohanty, P. P. Sarangi, D. P. Sahoo and K. Parida, Improving Charge Carrier Separation through S-Scheme-Based 2D–2D WS2/Sulfur-Doped g-C3N4 Heterojunctions for a Superior

Photocatalytic O2 Reduction Reaction, *ACS Appl. Energy Mater.*, 2024, **7**, 6360–6375.

53 X. Sithole, L. Q. Qwabe and L. N. Dlamini, A double transition metal MXene/S-scheme heterojunction composite with improved photoelectrochemical and photocatalytic properties, *Mater. Today Commun.*, 2024, **40**, 110233.

54 A. K. Asih, R. D. Yetti and B. Chandra, Photodegradation of Antibiotic Using TiO2 as a Catalyst: A Review, *Int. J. Pharm. Sci. Med.*, 2021, **6**, 37–43.

55 S. Atalay and G. Ersöz, *Novel catalysts in advanced oxidation of organic pollutants*, Springer, Cham, 2016, vol. 23.